J. Fluid Mech. (2014), *vol.* 751, *pp.* 255–297.
doi:10.1017/jfm.2014.304

Inertial wave excitation and focusing in a liquid bounded by a frustum and a cylinder

Marten Klein[1], Torsten Seelig[2], Michael V. Kurgansky[3], Abouzar Ghasemi V.[1], Ion Dan Borcia[2], Andreas Will[1], Eberhard Schaller[1], Christoph Egbers[2] and Uwe Harlander[2,†]

[1]Department of Environmental Meteorology, Brandenburg University of Technology Cottbus-Senftenberg, Burger Chaussee 2, D-03044 Cottbus, Germany

[2]Department of Aerodynamics and Fluid Mechanics, Brandenburg University of Technology Cottbus-Senftenberg, Siemens-Halske-Ring 14, D-03046 Cottbus, Germany

[3]A. M. Obukhov Institute of Atmospheric Physics, Russian Academy of Sciences, Pyzhevsky 3, 119017 Moscow, Russian Federation

(Received 29 August 2013; revised 28 March 2014; accepted 23 May 2014; first published online 18 June 2014)

The mechanism of localized inertial wave excitation and its efficiency is investigated for an annular cavity rotating with Ω_0. Meridional symmetry is broken by replacing the inner cylinder with a truncated cone (frustum). Waves are excited by individual longitudinal libration of the walls. The geometry is non-separable and exhibits wave focusing and wave attractors. We investigated laboratory and numerical results for the Ekman number $E \approx 10^{-6}$, inclination $\alpha = 5.71^\circ$ and libration amplitudes $\varepsilon \leqslant 0.2$ within the inertial wave band $0 < \omega < 2\Omega_0$. Under the assumption that the inertial waves do not essentially affect the boundary-layer structure, we use classical boundary-layer analysis to study oscillating Ekman layers over a librating wall that is at an angle $\alpha \neq 0$ to the axis of rotation. The Ekman layer erupts at frequency $\omega = f_*$, where $f_* \equiv 2\Omega_0 \sin\alpha$ is the effective Coriolis parameter in a plane tangential to the wall. For the selected inclination this eruption occurs for the forcing frequency $\omega/\Omega_0 = 0.2$. For the librating lids eruption occurs at $\omega/\Omega_0 = 2$. The study reveals that the frequency dependence of the total kinetic energy K_ω of the excited wave field is strongly connected to the square of the Ekman pumping velocity $w_E(\omega)$ that, in the linear limit, becomes singular when the boundary layer erupts. This explains the frequency dependence of non-resonantly excited waves. By the localization of the forcing, the two configurations investigated, (i) frustum libration and (ii) lids together with outer cylinder in libration, can be clearly distinguished by their response spectra. Good agreement was found for the spatial structure of low-order wave attractors and periodic orbits (both characterized by a small number of reflections) in the frequency windows predicted by geometric ray tracing. For 'resonant' frequencies a significantly increased total bulk energy was found, while the energy in the boundary layer remained nearly constant. Inertial wave energy enters the bulk flow via corner beams, which are parallel to the characteristics of the underlying Poincaré problem. Numerical simulations revealed a mismatch between the wall-parallel mass fluxes

† Email address for correspondence: uwe.harlander@tu-cottbus.de

near the corners. This leads to boundary-layer eruption and the generation of inertial waves in the corners.

Key words: boundary-layer structure, geophysical and geological flows, waves in rotating fluids

1. Introduction

Inertial waves appear as coupled pressure–velocity oscillations in a homogeneous fluid under constant uniform rotation. The restoring force is due to the Coriolis effect. Wave frequencies are band-limited to $(0, 2\Omega_0)$, where Ω_0 denotes the constant angular velocity of the system. Inertial waves are of importance in liquid planet cores (Tilgner 2009), but also in the deep ocean or the well-mixed equatorial atmosphere where stratification is weak (Harlander & Maas 2007*a*; Maas & Harlander 2007). But even in industrial rotating flows and spacecraft design (Agrawal 1993) they need to be considered. The waves transport momentum and can, roughly speaking, generate mean flows by angular momentum mixing (Maas 2001). Inertial waves have some striking properties, which can be attributed to their dispersion relation (e.g. Lighthill 1978, p. 438)

$$\omega = \pm \frac{2\boldsymbol{\Omega}_0 \cdot \boldsymbol{k}}{|\boldsymbol{k}|}, \tag{1.1}$$

with ω the wave frequency and $\boldsymbol{k}$ the wave vector. The wave frequency does not depend on the length of the wave vector, but on its direction. This implies that inertial waves of frequency ω propagate along a characteristic cone (Messio *et al.* 2008). Their phase velocity $\boldsymbol{c}_p$ is perpendicular to the group velocity $\boldsymbol{c}_g$. By fulfilling $\boldsymbol{c}_p + \boldsymbol{c}_g = \pm 2\boldsymbol{\Omega}_0/|\boldsymbol{k}|$, the waves show anomalous reflection from oblique boundaries (Phillips 1963; Maas 2001; Manders & Maas 2003; Harlander & Maas 2007*b*; Borcia & Harlander 2012).

Inertial waves can be excited in different ways. McEwan (1970) used a cylindrical tank rotating with angular velocity Ω_0 about its vertical axis. The top lid of the tank had a slight inclination with respect to the horizontal and rotated with angular velocity Ω that slightly differed from Ω_0. For instance, Maas (2001) and Swart *et al.* (2010) used a time-dependent rotation rate of the form

$$\Omega(t) = \Omega_0 \left[1 + \varepsilon \sin(\omega t)\right], \tag{1.2}$$

where ε is the non-dimensional velocity amplitude and ω is the frequency of the forcing. In the astrophysical context this kind of wave excitation is called longitudinal or zonal libration. Many librating planets or moons are believed to possess a liquid core (like the Earth's moon) or liquid layers in the form of subsurface oceans, e.g. Saturn's moons Titan and Enceladus (Noir *et al.* 2009). Libration-induced flow has been studied by several authors for different geometries. In the geophysical and astrophysical context it is obvious to use spheres (Aldridge & Toomre 1969; Busse 2010; Sauret, Cébron & Le Bars 2013; Zhang *et al.* 2013) or spherical shells (Tilgner 2007; Noir *et al.* 2009; Calkins *et al.* 2010; Koch *et al.* 2013; Sauret & Le Dizès 2013). Other geometries, such as cylinders (Noir *et al.* 2010; Swart *et al.* 2010; Lopez & Marques 2011, 2014; Sauret *et al.* 2012), cones (Beardsley 1970), prisms (Maas 2001) and boxes (Boisson *et al.* 2012) have also been studied. These models

are of general interest, even if seeming remote from geophysics at first glance. Waves themselves can drive strong mean flows (Maas 2001; Tilgner 2007; Bordes *et al.* 2012), but even without inertial waves mean flows can be driven by libration (Busse 2011; Sauret *et al.* 2012; Sauret & Le Dizès 2013). In the latter case nonlinearities in the Ekman boundary layer are responsible for the flows, but not inertial waves or local instabilities. It is thus important to carefully distinguish the different causes.

The geometry has a large effect on the flow induced by libration. For the sphere and the straight cylinder normal modes exist in the inviscid case. In contrast, for the spherical shell, the cone, the frustum or the prism, inviscid solutions become singular along detached shear layers, so-called wave attractors (Maas & Lam 1995; Rieutord & Valdettaro 1997; Maas 2001), which we shall discuss later in more detail. The surprising sensitivity to the confinement geometry is related to the hyperbolic nature of the underlying boundary value problems (Harlander & Maas 2007*a*). A container that is metrically simpler than a spherical shell but possesses most of its interesting features is an annulus whose inner cylinder is replaced by a truncated cone, called frustum in the following (Beardsley 1970; Henderson & Aldridge 1992). It is an annular version of the prism used by Maas (2001) in order to allow emergence of a unidirectional azimuthal mean flow. This geometry has been used earlier already by Swart *et al.* (2010) to experimentally study inertial-gravity wave excitation in analogy to the waves excited at ocean shelves. They observed a prominent wave beam excited in the corner between the sloping and the inner wall (foot of the shelf). This was explained by a local boundary-layer eruption similar to the eruption found at the critical latitude on the inner sphere of a librating spherical shell (Kerswell 1995; Koch *et al.* 2013) or at the shelf edge (Gostiaux & Dauxois 2007). Note that in both of the latter cases the boundaries at which waves are excited are convex (bending inwards). At the critical latitude (critical slope) the excited wave rays are tangent to the surface. In contrast, the bottom of the shelf studied by Swart *et al.* (2010) forms a concave boundary and the eruption gives rise to a wave beam perpendicular to the bottom, but emerges at the critical point. The three examples nicely illustrate how global oscillatory motions (of the boundary or the fluid) can lead to local wave excitation.

We study inertial wave excitation and wave attractors in an annulus with an inner frustum in the laboratory, by direct numerical simulation (DNS) and theoretical analysis. We librate either the frustum alone or the outer cylinder together with the top and bottom lids of the annulus. (In the laboratory the top and bottom lids are mounted on the outer cylinder so that they cannot move independently.) This is in a sense similar to the configuration of McEwan (1970). The advantage is that inertial waves are excited at predefined regions that depend on the boundaries that oscillate. This allows the different wave excitation mechanisms to be separated. Inertial waves are efficiently excited when fluid particles are forced to cross surfaces of constant angular momentum (in analogy to gravity waves that can be excited by pushing fluid particles across surfaces of constant density). We shall see that in the case of the librating inner wall an oscillating (rotary) Ekman layer forms on the frustum, due to which fluid moves periodically up and down the slope. When the outer cylinder and the lids librate, oscillating Ekman layers form over both lids and fluid moves periodically in radial direction. Both configurations result in a significant radial motion directed to or from a corner in a meridional section and can be suspected as the primary ingredient of inertial wave excitation. The effect of the librating outer cylinder on the wave motion is less clear. Usually, in studies with an entire tank librating, the Stokes and Stewartson layers at the vertical walls are

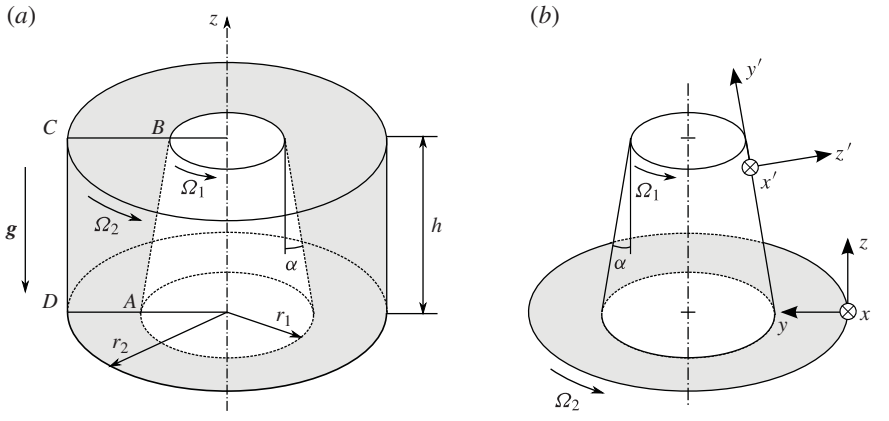

FIGURE 1. Schematic drawing of the annular tank. The inner wall (frustum) is inclined towards the vertical axes with an apex half-angle $\alpha = 5.71°$. (*a*) shows the set-up and (*b*) the local axes on the wall used for the boundary-layer analysis in § 5.1.

neglected or treated schematically (Wang 1970; Busse 2011). The main purpose of the present work is to study the different wave excitation mechanisms and to expand experimental and numerical results to clarify the role of the boundary layers on the wave excitation. Moreover, we study efficiency of wave excitation and how the latter depends on frequency.

The paper is organized as follows. In § 2 we describe the experimental and numerical set-ups. In § 3 we use ray tracing to discuss the wave patterns that can be expected. We also aim to single out forcing frequencies that yield geometrically simple solutions. In § 4 we compare experimental and numerical results for different forcing frequencies and the two forcing configurations. Subsequently, in § 5 we discuss the efficiency of wave excitation and study its frequency dependence. Finally, in § 6 we summarize our findings and give some concluding remarks.

2. Experimental and numerical set-up

The annular tank configuration is sketched in figure 1(*a*). It encloses a fluid volume of height h and height-dependent gap width $\Delta r(z) = r_2 - r_1(z)$. Rigid lids are located at $z = 0$ and $z = h$. The outer wall consists of a straight cylinder of radius r_2 and the inner wall is given by a frustum of radius

$$r_1(z) = r_1(0) - z \tan\alpha, \tag{2.1}$$

where $r_1(0)$ is the base radius and $\alpha = 5.71°$ is the apex half-angle of the frustum. The whole tank is mounted upright, so that the gravitational acceleration $\boldsymbol{g}$ is antiparallel to the rotation axis. In the present work we only consider constant mean rotation around the symmetry axis, i.e. $\boldsymbol{\Omega}_0 = \Omega_0 \boldsymbol{e}_z$.

The flow in the tank is described by the Navier–Stokes equations. Formulated for velocity $\boldsymbol{v}$ and pressure p in the corotating frame of reference the dimensionless equations read (e.g. Greenspan 1969, p. 7)

$$\frac{\partial \boldsymbol{v}}{\partial t} = -Ro\,(\boldsymbol{v}\cdot\boldsymbol{\nabla})\,\boldsymbol{v} - 2\boldsymbol{e}_z \times \boldsymbol{v} - \boldsymbol{\nabla} p + E\nabla^2 \boldsymbol{v}, \tag{2.2}$$

$$\boldsymbol{\nabla}\cdot\boldsymbol{v} = 0, \tag{2.3}$$

where Ro is the Rossby number and E is the Ekman number. Here the latter are defined as

$$Ro = \frac{U}{\Omega_0 h}, \quad E = \frac{\nu}{\Omega_0 h^2} \tag{2.4a,b}$$

where U is the velocity scale, h the length scale and ν the kinematic viscosity. As time scale we use $T = \Omega_0^{-1}$ due to the Coriolis effect. Deviations from rigid-body rotation are of the order $O(\varepsilon)$ and are introduced by the wall libration. The velocity $U = \varepsilon h T^{-1}$ and pressure scale $p_0 = \varepsilon h^2 T^{-2}$ are thus consistent with (2.2). This is in fact the scaling for boundary-layer flow over a flat surface in which the amplitude ε is the Rossby number. We use this scaling for the discretized equations to have only a single length scale h.

Inertial waves are excited by longitudinal librations of subsets of the four bounding walls. The two complementary configurations that could be realized in the laboratory (cf. figure 1*a*) are (i) libration of the frustum, i.e. $\Omega_1 = \Omega(t)$, and (ii) libration of the outer cylinder together with the lids, i.e. $\Omega_2 = \Omega(t)$. The remaining walls were kept at constant rotation rate Ω_0. We require no-slip conditions by prescribing velocity at the walls. The wall is impermeable such that there is no flux through the boundary.

Velocity components have to fulfill Dirichlet boundary conditions. These are homogeneous for components v_z and v_r, i.e.

$$v_z = v_r = 0 \quad \text{at } z = 0, h \text{ and } r = r_1(z), r_2. \tag{2.5}$$

The two different configurations can be realized by appropriate expressions for the azimuthal velocity v_φ alone. In case of the librating frustum (i) we have

$$\left.\begin{array}{ll} v_\varphi = 0 & \text{at } z = 0, h \text{ and } r = r_2, \\ v_\varphi = \varepsilon r \sin \omega t & \text{at } r = r_1(z), \end{array}\right\} \tag{2.6}$$

whereas libration of the outer cylinder and lids (ii) means

$$\left.\begin{array}{ll} v_\varphi = \varepsilon r \sin \omega t & \text{at } z = 0, h \text{ and } r = r_2, \\ v_\varphi = 0 & \text{at } r = r_1(z). \end{array}\right\} \tag{2.7}$$

(Selecting $Ro = \varepsilon$, cf. (2.4), demands rescaling of the boundary conditions so that ε will be dropped from (2.6) and (2.7).) The librational forcing is purely azimuthal, which makes the wall velocity $\boldsymbol{v}_w$ divergence-free. Both velocity and pressure need to be periodic in azimuthal direction and we require periodic Dirichlet conditions at $\varphi = 0, 2\pi$. Pressure is specified only up to an additive constant due to the remaining Neumann-type boundary conditions on boundaries in the (r, z)-plane.

It is worth noting that the numerical model offers more flexibility in the selection of boundary conditions than presented here. For the current work we have selected cases that are accessible with the laboratory set-up.

2.1. *Laboratory set-up*

2.1.1. *Apparatus design*

We constructed an apparatus with two corotating cylinders that can move individually. The outer cylinder wall is made out of borosilicate glass and has the height $h = 500$ mm, an outer-side diameter $2R = (415 \pm 5)$ mm and a wall thickness of $\Delta R = (7.0 \pm 1.5)$ mm. The axial-mean inner-side diameter is $2r_2 = (400.1 \pm 1.7)$ mm.

The frustum is made of aluminum and has a base diameter $2r_1(0) = 200$ mm and an upper diameter of $2r_1(h) = 100$ mm, corresponding to a half-apex angle $\alpha = 5.71°$. This rather shallow angle permits investigation of focusing reflections over a wide range of frequencies (cf. Borcia & Harlander 2012). The top lid is made of acrylic glass with a thickness of $\Delta h = 40$ mm and is mounted on the outer cylinder. The bottom lid is made of aluminum and rests on a turntable serving as support for the glass cylinder. All aluminum parts were anodized to suppress parasitic optical reflections and to make the surface resistant against chemical processes.

In the experiment we use a mean angular velocity of $\Omega_0 = \pi$ rad s^{-1}. Forcing amplitudes can be set within the interval $0 < \varepsilon \leqslant 0.49$, which is compliant with linear and weakly nonlinear regimes. We focused on forcing frequencies lying in the inertial wave band $(0, 2\Omega_0)$. The system was perturbed with a unique frequency ω, which immediately set the dominant frequency in the response spectrum of excited waves (similar to spectra shown by Sauret *et al.* 2012, 2013).

As working fluid we used water (density $\rho = 998.2$ kg m^{-3}, kinematic viscosity $\nu = 1.0028 \times 10^{-6}$ m^2 s^{-1} at 20 °C; see Grigull, Straub & Schiebener 1990). Visual observations were carried out after adding a small amount of a rheoscopic fluid. We used AQ-1000 from Kalliroscope, which is a suspension of microscopic crystalline platelets (Matisse & Gorman 1984). In accordance with Dominguez-Lerma, Ahlers & Canell (1985), 1–2 % polymeric flakes are immersed in a mixture of propylene glycol and water. The platelets align their longest axis parallel to the velocity shear present in the fluid. Under unidirectional illumination this results in a coherent reflection signal. Viewed from a fixed angle, the illuminated volume exhibits a shading that gives an impression of the streamlines and their evolution with time.

The set-up used for the optical measurements is shown in figure 2. We used an Nd:YAG laser to provide monochromatic light of 532 nm wavelength. The laser light-sheet is formed by a set of lenses and is approximately 200 mm wide and 2–3 mm thick. Measurements were conducted with the laser light-sheet illuminating the rectangular trapezoid ABCD illustrated in figure 2. In order to get a homogeneous light intensity across the whole slice (aspect ratio $\Delta r(0)/h = 1/5$), light from the horizontally mounted laser is redirected to be incident from the top. Flow patterns were then recorded as intensity distributions of the scattered light with a digital HD video camera, which was mounted at a physical distance of 500 mm normal to the illuminated slice.

2.1.2. *Measuring procedure and post-processing*

Each measurement was started by synchronizing both cylinders to rotate with the same angular velocity Ω_0. After the system reached rigid-body rotation, libration was switched on gradually. When the final libration amplitude was reached and transients had vanished the flow was recorded (cf. figure 2). Reaching stationarity usually took some tens of minutes. Individual record lengths were kept constant at 100 s for each selected point in the parameter space (ε, E, ω). A frame rate of 25 fps was used for all measurements. From each record 2500 images with a resolution of 720 pixels × 576 pixels were extracted, processed further by the procedure described in the following. Processing of the data was necessary to enhance the contrast of the oscillating patterns. The images were masked in order to exclude optical artifacts originating from optical reflections along the boundaries.

In all of the experiments conducted we were in a weakly nonlinear regime. Wave–wave and wave–boundary interactions yield the occurrence of harmonics $\omega_j = j\omega$ $(j = 0, 2, 3, \ldots)$ of the forcing frequency ω, where $\omega_j < 2\Omega_0$ for patterns related to inertial

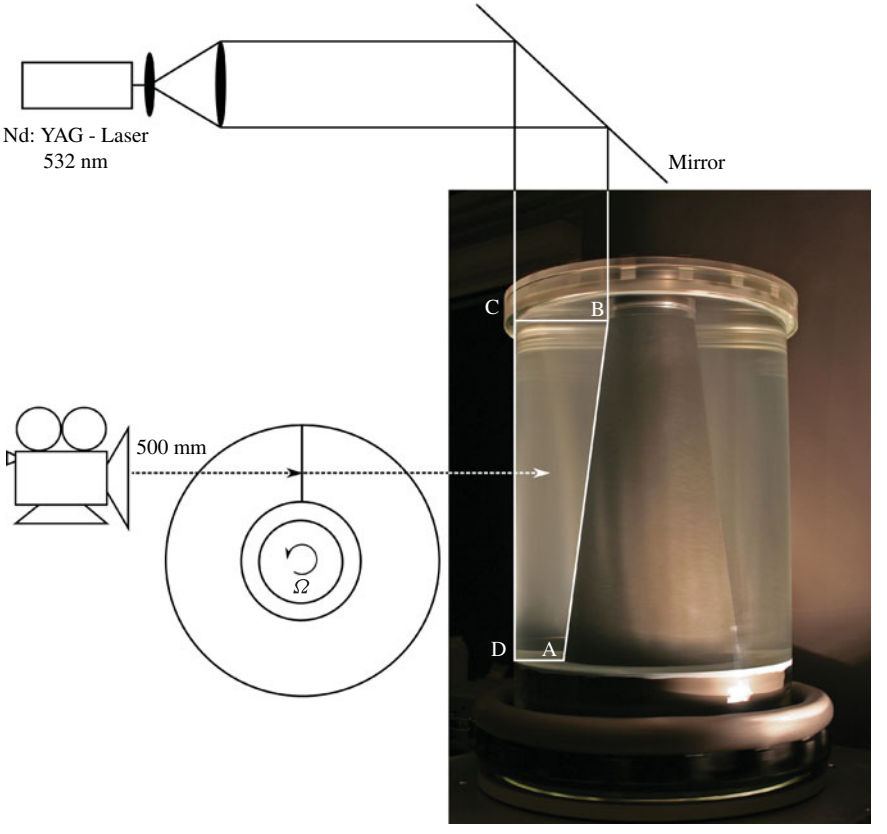

FIGURE 2. (Colour online) Experimental set-up in the laboratory. A laser light-sheet illuminates a slice ABCD of the fluid volume. The flow is visualized by recording light scattered from immersed platelets that are oriented according to the velocity shear in the fluid. The camera is positioned normal to the light sheet and records the evolution of streamlines in the meridional plane.

waves. The parameter setting permits filtering of the data at a few harmonics ω_j in order to suppress optical noise, which stems from imperfectness of the glass cylinder, inhomogeneous illumination, varying particle densities, etc. Because the phases and sampling rates of the individual constituents ω_j are unknown, we chose the flexible method of harmonic analysis as described by Emery & Thomson (2001), assuming that the physical signal lies on the frequency comb of harmonics $\omega_j = j\omega$. In essence, a truncated Fourier series is fitted to the time series containing all of the multiples ω_j in the inertial wave band. The residual $\boldsymbol{R}$ is computed for every point. In matrix form we may write

$$\boldsymbol{R} = \sum_{i=1}^{N} \left[\boldsymbol{Y}(t_i) - \left(\boldsymbol{A}_0 + \sum_{j=1}^{M} \boldsymbol{A}_j \cos \omega_j t_i + \boldsymbol{B}_j \sin \omega_j t_i \right) \right]^2 . \tag{2.8}$$

On the right-hand side $\boldsymbol{Y}(t_i)$ denotes data vector for the time slices $i = 1, 2, \ldots, N$, whereas $\boldsymbol{A}_0$, $\boldsymbol{A}_j$ and $\boldsymbol{B}_j$ for $j = 1, 2, \ldots, M$ are the Fourier coefficients of the harmonics obtained by a least-squares fit. With the aid of the Fourier coefficients the time

dependency of the flow patterns can be reconstructed. Individual harmonics can be accessed by computing amplitudes $\boldsymbol{D}_j = (\boldsymbol{A}_j^2 + \boldsymbol{B}_j^2)^{1/2}$ and phases $\boldsymbol{E}_j = \arctan(\boldsymbol{B}_j/\boldsymbol{A}_j)$, where $\boldsymbol{E}_j \in (-\pi, \pi]$. Evaluation of the residual $\boldsymbol{R}$ may serve as an estimate for quality of the projection and the anharmonic remainder.

2.2. *Numerical model*

Two aspects have been regarded as particularly important in the investigation of wave attractors: (i) the strong velocity gradients near the attractor and (ii) the propagation time of the waves needed to develop an attractor. The first is addressed by DNS. According to Moin & Mahesh (1998) this requires high accuracy, computational efficiency and conservation of the integrals of motion. Long simulation times require a numerical scheme with no or negligible numerical diffusion of the kinetic energy of the waves. With the following scheme all these requirements can be fulfilled.

The set of (2.2) and (2.3) is solved in a terrain-following locally orthogonal coordinate system (see appendix A for details). The model variables are staggered contravariant volume fluxes. The base version of the solver used was developed by Choi (1993) and Choi, Moin & Kim (1993) in the early 1990s for planar channel flows over small-scale topography. Kaltenbach *et al.* (1999) further developed the code for two-dimensional (2D) airfoil and large-eddy simulations (LES), focusing on asymmetric planar diffuser flow. The solver was further developed by AW (né Hauschild) and Kaltenbach in order to simulate diffuser flows with rotational symmetry (Akselvoll & Moin 1996; Verzicco & Orlandi 1996). At the present it still relies on the second-order central-differences scheme. Coriolis force, time-dependent wall boundary conditions, as well as factoring of viscous terms in the axial direction have been introduced in order to simulate libration-induced flows in the annulus in the corotating frame of reference.

Following Morinishi *et al.* (1998) it is important to note that the numerical scheme conserves mass and momentum *a priori* up to the individual orders of accuracy. It was also shown that the scheme will become fully conservative by conserving kinetic energy if a locally orthogonal grid is provided. The grid was optimized in this respect yielding the residual (in a discrete sense) of $\max_{i,j}(\Delta\alpha_{ij}) \approx 0.03^\circ$ taken over all grid lines $0 \leqslant i \leqslant N_r$, $0 \leqslant j \leqslant N_z$. One should note that the numerical model requires approximations in the geometry in the vicinity of the corners A and B due to local orthogonality. Hence, the linear ramp $r_1(z)$ forming the frustum wall is required to have smooth slope transitions near A and B thus introducing curvature in the axial direction (see figure 3(*b*,*c*) and appendix B for details).

In our implementation only the volume fluxes q^1 and q^2 lying in the (r, z)-plane are staggered. The volume flux q^3 is collocated with the pressure p at cell centres. Axisymmetry is exploited by the spectral derivative in the azimuthal direction. This is efficient in cases dominated by small azimuthal wavenumbers. Staggering resolves the discontinuous boundary conditions at the corners A–D (cf. (2.6) and (2.7)) up to one half of a grid cell. This is in contrast to manual regularization needed in other schemes (like Czarny *et al.* 2003).

We use a semi-implicit scheme for time integration. Only the wall-normal viscous terms are treated implicitly using a factored Crank–Nicolson scheme that is second-order accurate (Choi 1993). It is applied to avoid time-step limitations owing to viscous dominance in highly refined meshes. Advection, Coriolis force, pressure gradient, viscous cross and azimuthal derivatives, as well as boundary conditions are integrated with the third-order Runge–Kutta scheme described by Orlandi (2000).

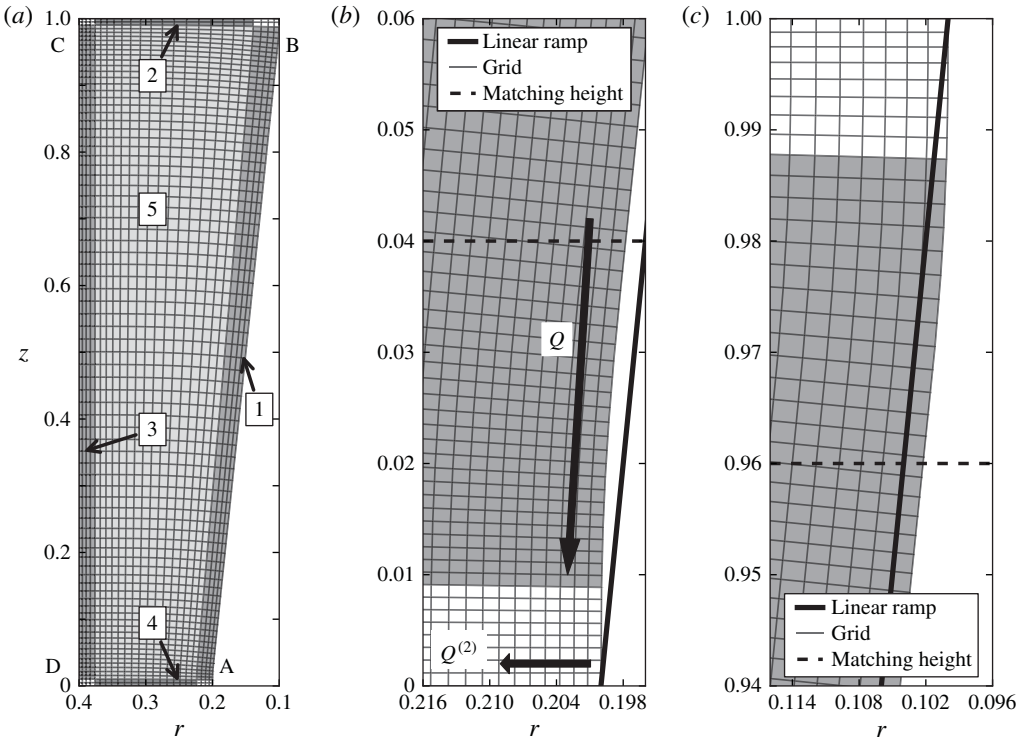

FIGURE 3. (*a*) Grid and subdomains: a generic structured grid is plotted for the trapezoid ABCD shown in figure 1(*a*) with $N_r \times N_z = 192 \times 640$ grid boxes in the (r, z)-plane. To aid visibility, only every eighth grid line is shown here. (*b*) Close-up at A and (*c*) close-up at B: enlarged view of the corners A and B, resolving every second grid line. Polynomial slope transitions of width $\Delta z = 0.04$ (matching heights) replace the top and bottom parts of the otherwise linear ramp. Shaded areas and numbers indicate subdomains used for computation of volume integrals. Here, $\boldsymbol{Q}$, $\boldsymbol{Q}^{(2)}$ exemplary show Ekman fluxes induced in the prograde phase for the frustum in libration (cf. § 5).

Since radial and axial dimensions are wall-bounded, alias removal is implemented for the periodic azimuthal direction only. We use a grid-shift method proposed by Canuto *et al.* (1991) for all dynamic variables and filter the Nyquist wavenumber explicitly.

The time steps had to be selected in such a way that time integration is stable and accurate. It is bounded by the CFL condition of the scheme and the fastest wave in the excited spectrum. Inertial waves are the only waves exhibited by the model. Given a plane wave with wave vector $\boldsymbol{k}$, we infer that phase velocity c_p and group velocity c_g are of the order of the wavelength $\lambda = |\boldsymbol{k}|^{-1}$. Hence the fastest wave has the maximum wavelength $\lambda_{max} \lesssim 2h$. Excited waves typically have much smaller wavelengths though, which will become more clear in § 4. Hence, $\lambda = 2h$ yields a pessimistic estimate for Δt, whereby a too large time step affects the high-wavelength end of the spectrum. In the configurations investigated it turns out that advection velocities are typically smaller than the maximum wave speed, $|\boldsymbol{v}| \ll \max(c_p, c_g)$. Thus, we take $\Delta t \lesssim C \Delta s_{min}$ initially, where Δs_{min} is the diameter of the smallest grid cell and C is the CFL number. (Note that we have to formally replace $C \to \varepsilon C$ for the scaled equations.) This yielded time steps of the order $\Delta t \simeq 2\pi \times 10^{-3}$. Estimation of the viscous frictional

time scale revealed that it is of similar order as the explicit time step, which means that inaccuracies of the implicit terms are sufficiently small.

3. Ray tracing

Ray tracing is a useful technique to qualitatively understand the structure of the flow field (Maas 2005), especially if the eigenspectrum is unknown. Analogue situations arise in quantum chaos, where classical billiards are used to infer properties of eigenfunctions of the Schrödinger operator in quantum billiards (see Ott 1993 for an introduction). In essence, ray tracing is able to capture wave-related features by a minimum of computational cost since no eigenvalue problem has to be solved and only a map has to be iterated. In many cases these characteristics correspond to the group velocities (Maas & Lam 1995; Maas 2001), i.e. the directions along which kinetic energy can propagate (Harlander & Maas 2006). In non-separable geometries so-called wave attractors arise. A wave attractor is a geometric object inside the cavity onto which all rays for a fixed frequency ω are focused, when the number of reflections exhibited by the ray tends to infinity. Wave attractors are not only features of inviscid models but can be found also in viscous eigenfunctions of the linearized Navier–Stokes operator (Rieutord & Valdettaro 1997).

The geometry of the annular cavity suggests to write the dimensionless (2.2) and (2.3) in cylindrical coordinates (see Borcia & Harlander 2012, and references therein). After linearization and elimination of the velocity we obtain for the pressure

$$\frac{\partial^2 p}{\partial r^2} - \left(\frac{4}{\omega^2} - 1\right)\frac{\partial^2 p}{\partial z^2} + \frac{1}{r}\frac{\partial p}{\partial r} + \frac{1}{r^2}\frac{\partial^2 p}{\partial \varphi^2} = 0. \tag{3.1}$$

The boundary conditions are due to impermeability of the walls, say $\boldsymbol{v}\cdot\boldsymbol{n} = 0$ at $z = 0,\ 1$ and $r = r_1(z),\ r_2$. Note that ω is from now on dimensionless and in the range $(0,\ 2)$. Writing the boundary conditions in terms of pressure we obtain

$$\frac{\partial p}{\partial z} = 0 \quad \text{at } z = 0,\ 1, \tag{3.2}$$

$$\mathrm{i}\omega\left[\frac{\partial p}{\partial r} - \left(\frac{4}{\omega^2} - 1\right)\frac{\partial p}{\partial \varphi}\tan\alpha\right] + \frac{2}{r}\frac{\partial p}{\partial \varphi} = 0 \quad \text{at } r = r_1(0) - z\tan\alpha, \tag{3.3}$$

$$\mathrm{i}\omega\frac{\partial p}{\partial r} + \frac{2}{r}\frac{\partial p}{\partial \varphi} = 0 \quad \text{at } r = r_2. \tag{3.4}$$

Characteristics of (3.1) form a double cone (e.g. Greenspan 1969). Symmetry permits us to consider only the $(r,\ z)$-plane, where it was shown by Borcia & Harlander (2012) that characteristics $c_\pm$ are described by

$$c_\pm = z \pm r\sqrt{\frac{4}{\omega^2} - 1}. \tag{3.5}$$

From a local source that emits waves with frequency ω, four ray directions can be found: upwards to the right, upwards to the left, downwards to the right, downwards to the left. The angle γ between the r direction and the ray is given by $\tan\gamma = (4/\omega^2 - 1)^{1/2}$ and is fixed by the frequency ω, which is a direct consequence of the dispersion relation. The wavelength does not enter the characteristic equation so that the reflection law of inertial waves differs from Snell's light reflection law. For inertial waves the angles between rotation vector and any wave rays (incident or reflected) are the same for a fixed wave frequency ω. The slope of the wall from which the waves are reflected does not determine the direction of the reflected ray. After a reflection on an inclined wall the wave can be focused or defocused

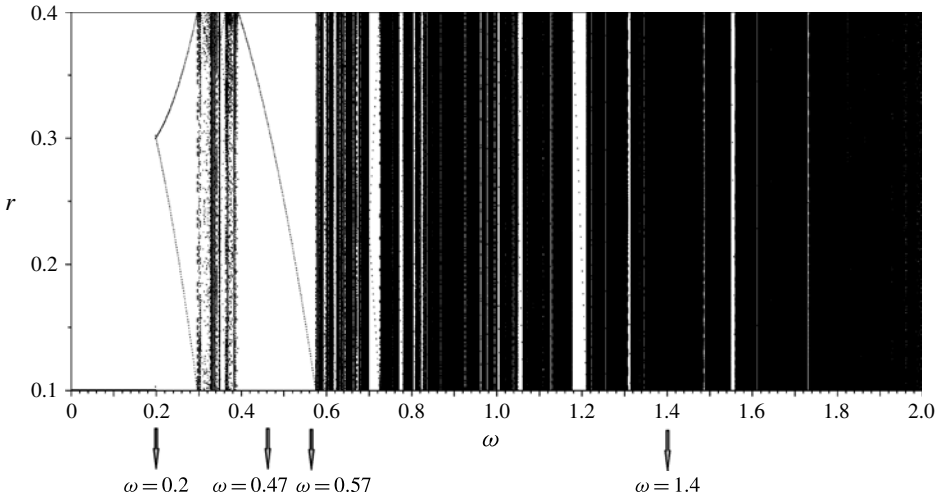

FIGURE 4. Ray-tracing estimate of the inviscid spectrum. The Poincaré diagram shows the reflection points along r (bottom lid) as a function of the wave frequency. The white regions ('windows') correspond to wave attractor bands. Frequencies considered in § 4 are marked: $\omega = 0.2$ (inclination of characteristics roughly coincides with the frustum wall), $\omega = 0.47$ and $\omega = 0.57$ (the middle and the upper limit of the 1/1 attractor interval) and $\omega = 1.4$ (collapsed interval that is a reminiscent of a normal mode solution; see also figure 9 in Borcia & Harlander 2012).

(see Phillips 1963). A (de)focusing reflection abruptly increases (decreases) the wavenumber and increases (decreases) the energy density of a wave beam ($E > 0$ case). In general, closed trajectories in the form of wave attractors are obtained if focusing dominates over defocusing after multiple reflections from the inclined wall (see Maas & Lam 1995).

A proper way to display wave attractor frequencies is to construct a Poincaré diagram such as that shown in figure 4. For a large number of different frequencies the ray-tracing paths were calculated. Without loss of generality, we consider just the reflections at the upper lid and outer cylinder wall. After waiting for the 5000th reflection we plotted the reflection point coordinates along the selected r- and z-axis up to the 20 000th reflection. In a generic setting, no low-order wave attractor exists and wave rays cover, roughly speaking, the entire available domain. Consequently, a black line forms for the selected frequency ω along the Poincaré surface as can be seen in figure 4 (r-axis only; the z-axis the diagram is qualitatively similar). However, in some particular frequency intervals focusing dominates and only a few reflection points exist. These frequency intervals correspond to low-order wave attractors, appearing as 'windows' in the otherwise black diagram. By wave attractor band (window) we refer to frequency intervals in which a certain geometric structure with a constant (small) number of reflections exists. A single structure obtained for a selected ω is representative of the corresponding wave attractor class $I_{m/n}$, where m denotes the number of reflections along r and n those along z. The class $I_{m/n}$ exists on the corresponding frequency interval $I_{m/n} \subset (0, 2)$ of non-zero measure. A few examples are shown for $\omega = 0.2, 0.47, 0.57$ in figures 6–8(a). All of these frequencies are located within a wave attractor window of figure 4. Note that waves trapped on the simplest possible 1/1 wave attractor propagate in the clockwise direction (focusing reflections dominate), which is indicated by the arrows.

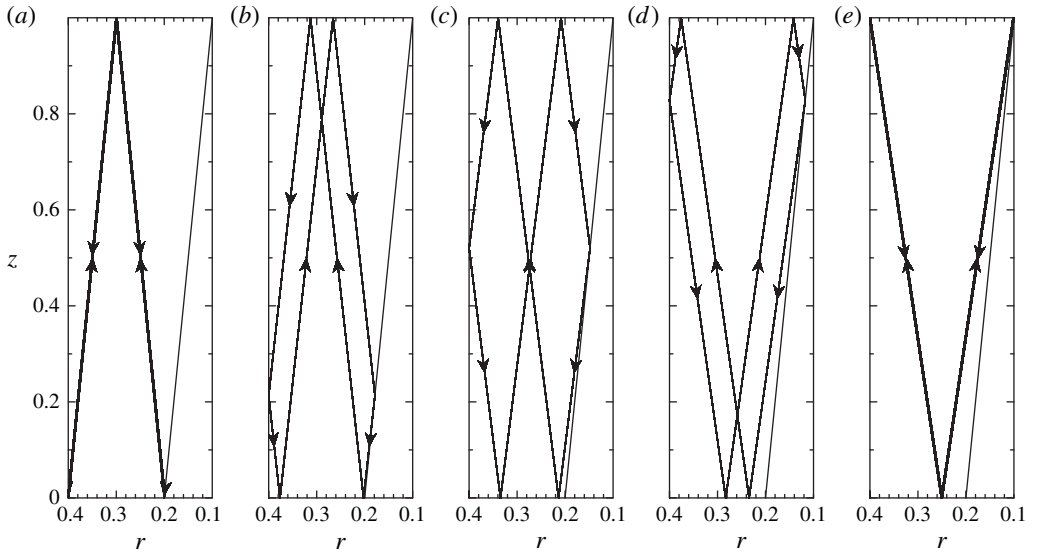

FIGURE 5. Theoretical results for the inviscid case. Wave attractor solutions for the limiting frequencies and intermediary states of the class $I_{2/1}$. The images were obtained by launching a characteristic ray at an arbitrary point, letting it reflect 5000 times and plotting the next 400 reflections: (*a*) $\omega = 0.2$; (*b*) $\omega = 0.22$; (*c*) $\omega = 0.25$; (*d*) $\omega = 0.28$; (*e*) $\omega = 0.296$.

Representatives of $I_{2/1} \approx [0.2, 0.296]$ (cf. figure 4) are shown in figure 5. Note that the attractors corresponding to the limit frequencies are degenerate, i.e. at each point on the attractors shown in figure 5(*a*,*e*) wave rays propagate in both directions. In the case of finite viscosity, interference of wave beams has to be expected, which is beyond ray tracing. When the frequency is increased from the lower limit, a 'two-cell structure' appears and becomes symmetric with respect to the r- and z-axes for $\omega \approx 0.25$. The attractor path is separated such that in a generic point wave rays are propagating in a single direction only (see arrows). For higher frequencies the cells become more elongated in the z direction and vanish again for the upper limit frequency. It should be noted that figure 5(*d*,*e*) are approximately mirrored versions of figure 5(*a*,*b*). Note further that the lower limit $\omega = 0.2$ also is the critical frequency that separates 'point attractors' located in the upper right corner B of the domain from wave attractors in the whole annulus (cf. figure 4). Actually, for $\omega = 0.2$ the wave rays have the same slope as the frustum. Thus, in linear theory, any wave with $\omega < 0.2$ reflected from the frustum would lead to an infinite wave energy density in the upper right corner B.

When focusing and defocusing exactly compensate for each other (m even and n odd), one finds a periodic orbit that is not a wave attractor (Manders & Maas 2003). The shape of the periodic orbit depends on the starting point (in contrast to wave attractors). The two limiting ray patterns (in terms of figure 5) exist for the same frequency ω ('collapsed window'). These are typical features indicating existence of a normal mode solution at this frequency. One can say that such frequencies are remnants of the discrete (inviscid) eigenspectrum. An example of such a 'surviving' eigenmode frequency is $\omega = 1.4$ (see figure 9(*a*), where the 'limiting' periodic orbits connect corners A and B or C and D by a tilted W-like pattern).

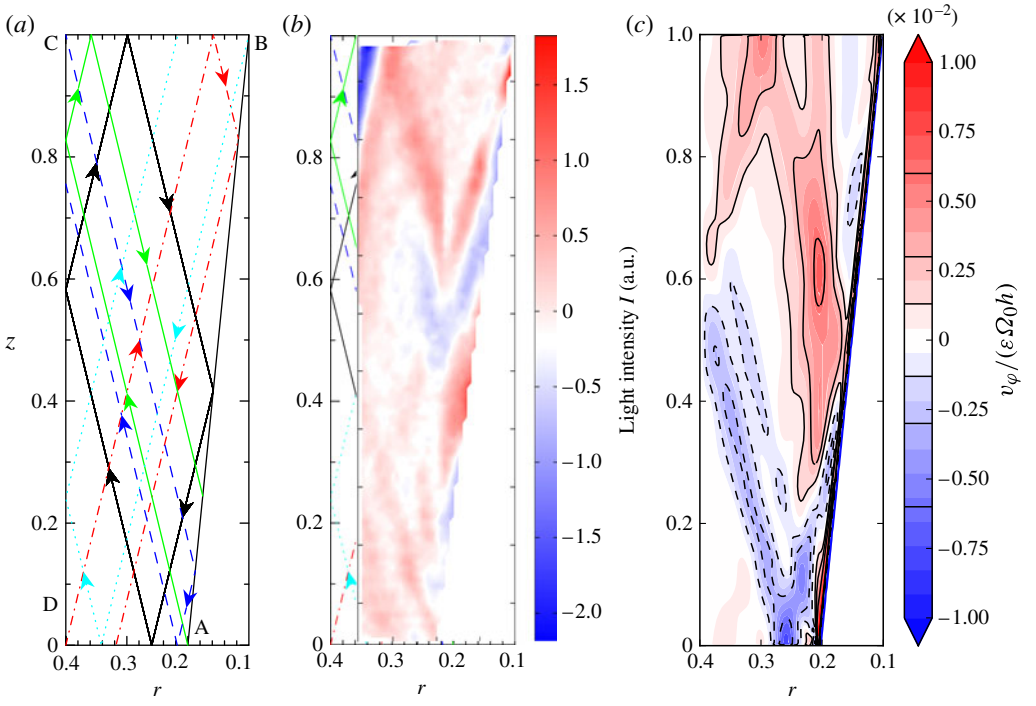

FIGURE 6. (Colour online) Comparison between (*a*) the ray tracing, (*b*) measurement and (*c*) simulation for the excitation frequency $\omega = 0.47$ at $E = 1.3 \times 10^{-6}$, $\varepsilon = 0.2$ for the librating frustum. In (*c*) the boundary-layer flow exceeds the scale by a factor of 20; solid (dashed) lines distinguish positive (negative) values. Characteristic angles are in qualitative agreement.

The inertial frequency band (0, 2) is elaborately divided into bands $I_{m/n}$ of wave attractors, single points corresponding to periodic orbits and 'ergodic' regions. From figure 4 one can roughly say that the attractor windows become smaller and periodic orbits more dense as $\omega \to 2$.

4. Comparison of theory, experimental and numerical results

The relation between wave attractors obtained by ray tracing and the viscous eigenfunctions has been discussed in detail for the spherical shell by Rieutord & Valdettaro (1997) and Rieutord, Georgeot & Valdettaro (2001). For small Ekman numbers the modes are strongly localized with a clear correspondence to the ray patterns. The eigenspectra are rather dense. Thus, it is obvious that the viscous boundary value problem, even though elliptic, is dominated by the hyperbolic part of the operator. It should be noted that these findings are typical for non-separable domains and not limited to the spherical shell. The viscous eigenspectrum of the annulus bounded by a frustum is unknown, except for the few modes computed by Henderson & Aldridge (1992) for a slightly different geometry. We used ray tracing to estimate frequency intervals of inertial wave attractors adapting the picture of propagating inertial wave (packages). Thus, it would be interesting to see an eigenspectrum for our geometry and to compare it with the energy spectra found in the numerical simulations and experiments (cf. § 5.3). Note that non-separable cases

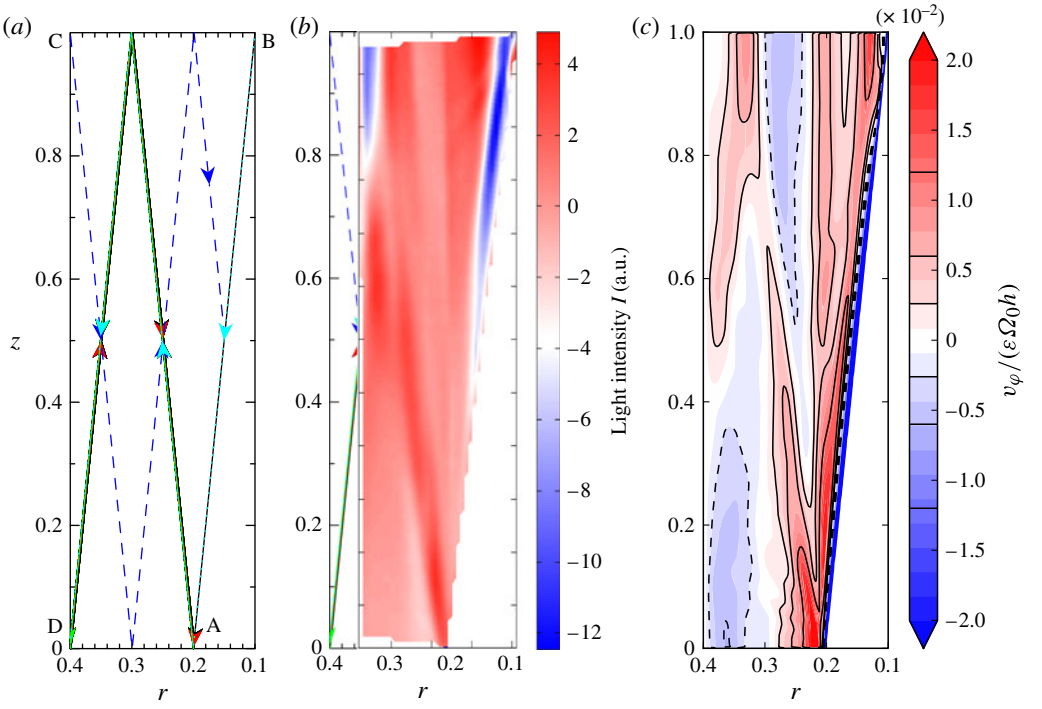

FIGURE 7. (Colour online) Comparison between (*a*) the ray tracing, (*b*) measurement and (*c*) simulation for the excitation frequency $\omega = 0.2$ at $E = 1.3 \times 10^{-6}$, $\varepsilon = 0.2$ for the librating frustum. In (*c*) the boundary-layer flow exceeds the scale by a factor of 10; solid (dashed) lines distinguish positive (negative) values. Characteristic angles are in qualitative agreement.

are closer to real-world applications, wherefore it is illuminating to study the former in detail.

In the following ray-tracing results are compared with measurements and simulations for the viscous, weakly nonlinear regime. Fixed parameters are the Ekman number $E = 1.3 \times 10^{-6}$ and geometry. In the laboratory, the libration amplitude $\varepsilon_{lab} = 0.2$ was kept constant, too. For the case of outer cylinder and lids in libration we adapted ε to keep the Rossby number based on the libration velocity constant. Hence, $\varepsilon_{num} = 0.2$ for the frustum in libration (as in the laboratory) and $\varepsilon_{num} = 0.1$ for the lids and outer cylinder in libration. Figures 6–9 show (*a*) the spatial structure of the solutions obtained by ray tracing, (*b*) projection amplitudes of light intensity measurements (in arbitrary units) and (*c*) the simulated azimuthal velocity field for different libration frequencies. In (*a*) we show in addition to the wave attractor (solid black line) also the four rays emerging from the corners: a (green online) solid line from the lower right corner A, a (magenta online) dotted line from upper right corner B, a (blue online) dash-dotted line from upper left corner C and a (red online) dashed line from lower left corner D. This is because of the localization of the forcing, which we discuss in § 5.

4.1. *Frustum libration*

Figure 6 shows the results for $\omega = 0.47$. The frequency falls in the 1/1 wave attractor window (cf. figure 4) and corresponds to the simplest possible wave attractor structure.

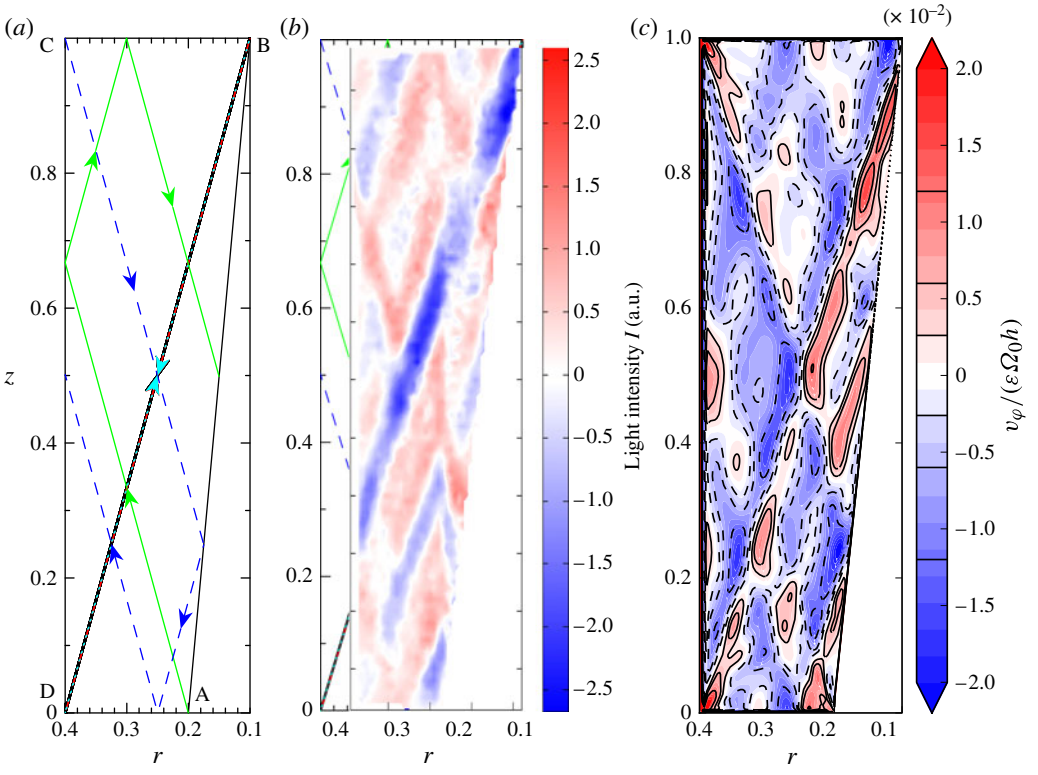

FIGURE 8. (Colour online) Comparison between (*a*) the ray tracing, (*b*) measurement and (*c*) simulation for the excitation frequency $\omega = 0.57$ at $E = 1.3 \times 10^{-6}$, $\varepsilon_{lab} = 0.2$, $\varepsilon_{num} = 0.1$ for lids librating together with the outer cylinder. In (*c*) the boundary-layer flow exceeds the scale by a factor of 10; solid (dashed) lines distinguish positive (negative) values. Characteristic angles are in qualitative agreement.

The unique diamond shape is easily recognized since it is the same structure found by Maas (2001) in a librating prism. In addition to the wave attractor itself, figure 6(*c*) exhibits the effect of focusing: spatial compression, an increase in velocity amplitude and a jump in phase (sign reversal). Furthermore, a slightly weaker and thinner beam originates from the corner A (bottom right) and runs parallel to the wave attractor. Considering the width of the wave beams, it takes practically just one round trip for this beam to reach the wave attractor. A second beam from corner B (top right) is also visible, but much weaker. This is easily explained by the radius ratio of $r_1(0)/r_1(h) = 2$ of the librating frustum that results in a smaller librational velocity amplitude at corner B. Note also the scaling of the velocity field in the corotating frame (divided by ε) and that the colour scale has been truncated to ± 0.01 to make interior features visible (indicated also by exceeding-range caps on the colour bar). In fact, the maximum azimuthal velocity of the frustum at corner A is approximately 20 times larger ($v_\varphi = 0.2$) and decays rapidly within the boundary layer. Note also that higher harmonics are not notable. This indicates that the corner beams (also found by Beardsley 1970; McEwan 1970; Sauret *et al.* 2012) are features of the linear dynamics. Numerical simulations show that the whole solution in the bulk remains similar for the linear forcing with $\varepsilon = 0.02$ and structures related to wave frequency $\omega = 0.47$ become more pronounced.

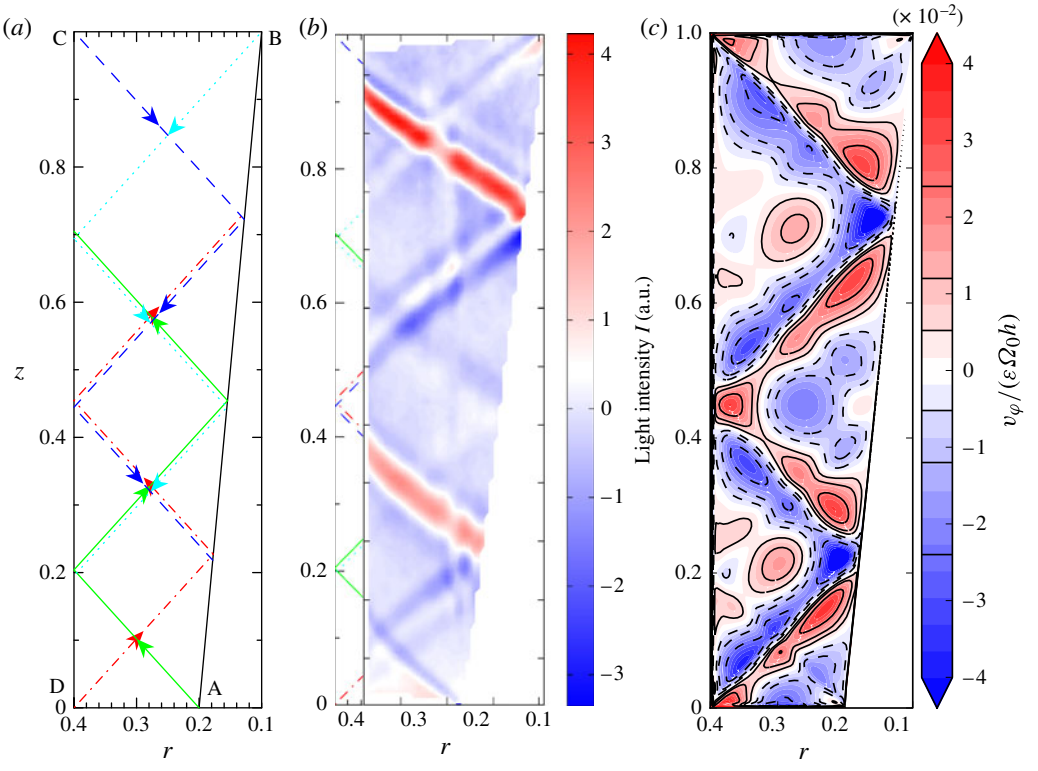

FIGURE 9. (Colour online) Comparison between (*a*) the ray tracing, (*b*) measurement and (*c*) simulation for the excitation frequency $\omega = 1.4$ at $E = 1.3 \times 10^{-6}$, $\varepsilon_{lab} = 0.2$, $\varepsilon_{num} = 0.1$ for lids librating together with the outer cylinder. In (*c*) the boundary-layer flow exceeds the scale by a factor of 5; solid (dashed) lines distinguish positive (negative) values. Characteristic angles are in qualitative agreement.

Measurements shown in figure 6(*b*) exhibit the same wave structures as numerics and ray tracing. It is apparent that measurements suffer from various errors, which apply equally also to figures 7–9(*b*) in this section. Characteristics are artificially and increasingly curved towards the outer cylinder. The outermost part of the cross-section ABCD is invisible due to total reflection of light at the curved glass–air interface. The invisible part has been replaced by rays of inviscid theory of § 3. Furthermore, laboratory measurements exhibit higher amplitudes in the upper half. This is due to scattering, absorption and expansion of the light sheet. All contribute to a slightly inhomogeneous axial light intensity (remember that light was incident from the top; cf. figure 2). Compared with the corresponding numerical simulation, corner beams are dominating, which can be attributed to decreasing velocity shear as the beam propagates and spreads due to viscosity (Cortet, Lamriben & Moisy 2010).

The wave attractor appears weaker than the one shown, for instance, by Maas (2001) for the librating prism. This is due to different reasons. (i) Measurements were done with immersed platelets and light intensities give an impression of shear rather than relative velocity. Other researchers used particle image velocimetry (PIV) instead. (ii) Often kinetic energy is used to magnify amplitudes related to waves, but this requires the velocity field to be known. (iii) The apex half-angle of the frustum is

small ($\alpha = 5.71°$), which results in a weak focusing. (iv) From the numerical results we recover excited wave amplitudes of $O(1\ \mathrm{mm\ s^{-1}})$. Other forcing mechanisms may be more efficient (e.g. that of Messio *et al.* 2008). (v) The regime $\varepsilon = 0.2$ already exhibits nonlinearity in the boundary layer, due to which higher harmonics $n\omega$ ($n = 2, 3, \ldots$ for $n\omega < 2$) are present and the wave attractor for ω appears less pronounced (see figures 8 and 11; but also Jouve & Ogilvie (2014) on that matter). Anyhow, the wave attractor predicted by ray tracing is clearly visible. Numerical simulations also revealed that such a simple pattern as the 1/1 wave attractor tends to vanish between $10^{-5} < E < 10^{-4}$. It depends also on ε, but this is generally in agreement with results published for the full cylinder. Sauret *et al.* (2012) and Lopez & Marques (2014) found distinct wave beams for $E = O(10^{-5})$, whereas Lopez & Marques (2011) for an equivalent Ekman number of $E = O(10^{-4})$ did not.

One last aspect we like to address is the vertical shear layer emerging from the bottom lid at $r_1(0)$. As can be seen in figure 6(*c*), this is a prograde mean flow layer of similar amplitude as the wave field. In the frequency-filtered measurements, figure 6(*b*), the shear layer occurs only as artifact (also visible in the figures 7–9*b*). The emergence from the lower corner A seems well in agreement with existing theory developed for the spherical shell by asymptotic methods (Sauret & Le Dizès 2013) (but for $\omega \gg 2$). Here the frustum resembles the upper half of the near-equator region of a sphere. The cause is nonlinearity in the boundary layer over a librating wall. This feature remains persistent also in the inertial wave band.

Figure 7 shows the flow patterns in the meridional section ($\varphi = \text{const.}$) for the critical frequency $\omega = 0.2$ that also separates 'point attractors' (here it is just the corner B) for $\omega < 0.2$ from wave attractors (one-dimensional objects) for $\omega > 0.2$. Wave rays have the same slope as the inner cone for this frequency and one expects a maximum of wave energy density along the slope due to boundary-layer eruption (cf. § 5). For this configuration we see a single inertial wave beam excited at the corner A in the figure 7(*b*,*c*). The wave amplitude is large along the slope and confined to the boundary, which is consistent with the inclination angle α matching the critical angle. The wave attractor expected from figure 7(*a*) is visible in the experimental and numerical results. For $\omega = 0.2$ the wave beam emerging from corner A is in principle directly fed onto the wave attractor.

An azimuthal mean flow at $r = r_1(0)$ is also visible in figure 7(*c*), similarly to $\omega = 0.47$. Note that there are no higher-harmonics visible. This shows that linear properties are still dominating. Another aspect relevant for the cases $\omega = 0.2, 0.47$ is that the corner beams are quite strong. Although inertial waves might be emitted along the whole oblique wall, their amplitude must be very small. At least, we could not detect such waves experimentally or numerically.

Until now the figures correspond to wave excitation by frustum libration. For this case excited wave amplitudes strongly decrease with forcing frequency as $\omega \to 2$ (see § 5).

4.2. *Lids plus outer cylinder libration*

Here we show a few examples of the complementary configuration, where the lids librate together with the outer cylinder and the frustum is held at constant rotation rate $\Omega_0 = 1$. As will be discussed in § 5, for this configuration it is in general more suitable to investigate frequencies larger than one. This comes at the expense of a much 'denser' spectrum of wave attractor bands and periodic orbits as can be seen in figure 4. Fixed parameters are now $E = 1.3 \times 10^{-6}$, $\varepsilon_{lab} = 0.2$ for the laboratory experiments and $\varepsilon_{num} = 0.1$ for the numerical simulations.

General features observed for outer cylinder and lids in libration is that corner beams emerge from all four corners A–D, which is in contrast to frustum libration (prominent at A, weak at B). The strongest beams originate from corners C and D due to the larger radius r_2 (cf. figure 8*c*). We begin with excitation frequency $\omega = 0.57$, which is the upper boundary of the 1/1 attractor window. In this case the limit cycle coincides with the least inclined diagonal, i.e. the black solid line in figure 8(*a*) that connects corners B and D. Even though the lids are of different size wave beam magnitudes are almost the same. In figure 8(*b*), however, the attractor seems to be more pronounced than the beam starting at C.

Figure 8(*c*) shows clear signs of nonlinearity. From the outer corners C and D emission of a 'wave beam fan' is visible, containing less inclined beams. Frequency filtering at $2\omega = 1.14$ and $3\omega = 1.71$ clearly isolates the respective beams (see in this respect § 2.1.2 and appendix C). The mechanism appears to be triggered by instability in the boundary layer. It develops first in the corner region and spreads along the outer cylinder wall if ε is increased (enhanced nonlinearity) or if ω is decreased (longer duration of stable and unstable libration phases). As $\varepsilon \to 1$ we can expect spontaneous emission of inertial waves to become more important (Sauret *et al.* 2012, 2013). This should not be confused with the mechanism resulting in wave beams excited in the corners. We reduced ε to 0.01 and still found the corner beams for the prescribed libration frequency ω, whereas higher harmonics disappeared.

Other interesting frequencies are those for which focusing and defocusing compensate. This is the case, for instance, if $\omega = 1.4$. Corresponding results are shown in figure 9. In this case all rays (including those originating from corners) lack net focusing and lie on a closed trajectory. In figure 9(*b*) optical distortion of the characteristics and masking of the outermost region is quite obvious. The structures closer to the frustum wall, however, can be clearly identified.

We close with noting that the mean flow layer (a layer of Stewartson-type) emerging at A is weaker here than for the frustum libration case (compare, for instance, figures 6*b*,*c* with 8*b*,*c*). The origin is the same: nonlinearity in the oscillating Ekman layer (Sauret & Le Dizès 2013).

5. Wave excitation

Simulations and observations revealed that dominating wave excitation is localized at the four corners A–D in the (r, z)-plane of the annular cavity (see examples in § 4). It was pointed out, for instance, by Wang (1970) and Busse (2010) that the corner regions in a librating full cylinder are not easily treated analytically even in an asymptotic limit without any waves. The underlying corner flow problem has been addressed recently by Swart *et al.* (2010), Boisson *et al.* (2012) and Sauret *et al.* (2012). The most distinct feature found by Swart *et al.* (2010) is a wave beam emitted due to boundary-layer eruption at the bottom of the sloping wall. No such beam was found at the free upper surface and it was speculated whether corners prevent boundary-layer eruption. Our results suggest that the absence of a boundary layer at the free surface prevents boundary-layer interaction and hence leads to a dominant wave beam at the bottom only. Although the details of the dynamics are not yet understood, we contribute to the ongoing discussion by investigating the mechanisms involved via splitting the problem into the discussion of boundary layer and bulk flow. We distinguish between frustum in libration and lids plus outer cylinder in libration, with the focus on the frequency dependence of wave excitation efficiency.

In general, a temporal snapshot for a weakly nonlinear setting is composed of dominant spatial structures that oscillate with harmonics $n\omega$ of the forcing frequency ω, where $n = 0, 2, 3, \ldots$ for $n\omega < 2$ (see § 4). The different structures can be separated according to their time dependency by applying the frequency filters described in § 2.1.2 or appendix C, respectively. From the examples presented above the system's temporal variability with respect to inertial waves is dominated by the structures corresponding to the forcing frequency ω. In the following we will therefore focus on the frequency-filtered fields.

5.1. *Boundary-layer analysis*

5.1.1. *Local equations*

We apply classical boundary-layer theory to the rotating annular cavity. Strictly, this assumption is valid only in the asymptotic limit without inertial waves present, but it may be justified also due to the scale separation between boundary layer and bulk flow (cf. figures 6–9). We neglect any feedback from the bulk flow to the boundary layer. With respect to wave excitation by libration this may be lesser a problem when we think of the libration-induced boundary layer providing the primary flow. The essentials of the following derivations are well-documented in different books, for instance, Batchelor (1967), Greenspan (1969) and Busse *et al.* (2007). We collect some aspects here for the sake of a uniform nomenclature.

As usual we restrict our attention to the linear limit ($\varepsilon \ll 1$) and focus on small Ekman numbers, $E \ll 1$. Owing to the latter, the generic boundary-layer depth δ_{BL} is much smaller than the length scale, i.e. $\delta_{BL} \ll h$. Also the radii fulfill $r_1, r_2 \gg \delta_{BL}$ and for the gap width $r_2 - r_1 \gg \delta_{BL}$ correspondingly. It is permissible to use a local Cartesian approximation on each of the walls, as is shown in figure 1(*b*). The tangential coordinates are (x', y', z') and the system is oriented such that z' points in wall-normal direction into the fluid (it is antiparallel to the surface normal $\boldsymbol{n}$). We let x' point in azimuthal (zonal) direction so that y' is the second wall-tangential component lying in the (r, z)-plane. Cylindrical velocities (v_r, v_φ, v_z) are mapped to (u', v', w'), where u' is the zonal velocity, w' the wall-normal velocity and v' is the second wall-tangential velocity. On the lids, the tangential axes (x', y', z') become parallel to an underlying Cartesian system that can be introduced locally as (x, y, z) as illustrated in figure 1(*b*). In some places this will be used to distinguishing between frustum (primed) and lid (unprimed).

Within a boundary layer it is well known that gradients in wall-normal direction z' are dominating, which means $\partial(\cdot)/\partial z' \gg \partial(\cdot)/\partial x', \partial(\cdot)/\partial y'$. Axisymmetry of the forcing and the geometry yields $\partial p/\partial x' \equiv 0$. Pressure can be eliminated by cross-differentiation of the tendencies for v' and w'. Introducing the poloidal (meridional) stream function ψ yields $v' = -\partial\psi/\partial z'$ and $w' = \partial\psi/\partial y'$. Subtraction of the tendencies, insertion of ψ and keeping only the wall-normal first-order spatial derivatives yields the reduced set of equations

$$\frac{\partial^3\psi}{\partial t\partial z'^2} = +f_*\frac{\partial u'}{\partial z'} + E\frac{\partial^4\psi}{\partial z'^4}, \qquad \frac{\partial u'}{\partial t} = -f_*\frac{\partial\psi}{\partial z'} + E\frac{\partial^2 u'}{\partial z'^2}. \tag{5.1a,b}$$

We introduced the effective Coriolis parameter $f_* \equiv f\sin\alpha$ with $f = 2$ the (dimensionless) conventional Coriolis parameter.

Equations (5.1) are appropriate for a fluid in the half-space $z' > 0$ bounded by a wall at $z' = 0$. On the bottom lid $\alpha = \pi/2$ and $f_* = f$, whereas on the top lid $\alpha = -\pi/2$ and

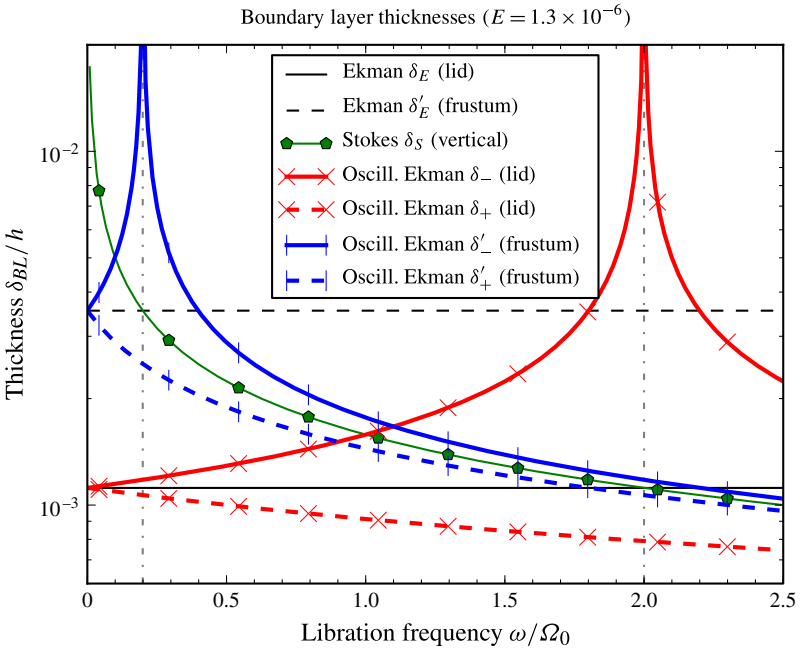

FIGURE 10. (Colour online) Comparison of the different classical boundary-layer depths and their dependence on the libration frequency. All plots are for the Ekman number $E = 1.3 \times 10^{-6}$. Classical Ekman layers δ_E, δ'_E are strictly valid only in the limit $\omega = 0$. Boundary layers over oscillating surfaces show eruptions (vertical dash-dotted lines). See the text for details.

$f_* = -f$. On the frustum $\alpha = 5.71°$ so that $f_* = 0.2$ and on the outer cylinder $\alpha = \pi$ and $f_* = 0$. Equations (5.1) state that inside a boundary layer the fluid is sensitive only to the wall-tangential ('horizontal') component of the Coriolis force.

No-slip conditions for the walls yield the boundary conditions $\psi = \partial\psi/\partial n = 0$ and $u' = U\sin(\omega t)$ at $z' = 0$. Here, U is the local amplitude of zonal velocity of the librating wall, i.e. $U = \varepsilon r$ with r the physical distance from the axis of rotation. In local Cartesian approximation, however, we treat U as constant.

5.1.2. *Classical Ekman and Stokes layers*

The classical Ekman problem is that of an interior geostrophically balanced flow $u'_{bulk} = U = \text{const.}$ over a wall with homogeneous no-slip condition (in the corotating frame). For not too small inclination angles $|\alpha|$ and requiring $|\boldsymbol{v}| < +\infty$, (5.1) have the solution (e.g. Busse *et al.* 2007)

$$u' = U\left[1 - \cos\left(\frac{z'}{\delta'_E}\right)\mathrm{e}^{-z'/\delta'_E}\right], \quad v' = \mathrm{sgn}(f_*)U\sin\left(\frac{z'}{\delta'_E}\right)\mathrm{e}^{-z'/\delta'_E}, \tag{5.2a,b}$$

where $\delta'_E \equiv \sqrt{2\nu/|f_*|} \geqslant \delta_E$ is the Ekman-layer thickness over the frustum (cf. figure 10; dashed horizontal line). For a horizontal lid with $\alpha = \pm\pi/2$ we have $\delta'_E = \delta_E$ (solid horizontal line). The depth of a classical Ekman layer is constant for all amplitudes U. Strictly, this is valid only in the limit $\omega = 0$. To aid visibility, the plots of δ_E and δ'_E shown span the whole ω range in figure 10. A typical time scale of the Ekman

layer formation is given by f_*^{-1} and depends on the inclination angle, from which we recover the well-known property that the energy dissipation rate $\mathrm{d}K/\mathrm{d}t$ is proportional to the kinetic energy K of the interior flow, i.e. $\mathrm{d}K/\mathrm{d}t \propto -|f_*|K$.

Along a vertical wall (outer cylinder) the time dependence of the interior flow or the boundary cannot be neglected since $f_* = 0$ (absence of an intrinsic time scale). For the librating outer cylinder (amplitude $U = \varepsilon r_2$) we expect the classical Stokes-layer solution (Batchelor 1967)

$$u' = U \sin\left(\frac{z'}{\delta_S} - \omega t\right) \mathrm{e}^{-z'/\delta_S} \tag{5.3}$$

with the Stokes-layer thickness $\delta_S \equiv \sqrt{2\nu/\omega}$, which exhibits a singularity at $\omega = 0$ (thin solid line in figure 10). Equation (5.3) states that only the zonal velocity component is non-zero.

5.1.3. *Oscillating Ekman layer*

Oscillatory (rotary) Ekman layers are well known in oceanography since tidal flows in a rotating frame commonly occur (see in this respect Prandle 1982; Thorade 1928). This is an analogue problem to the librating wall and the fluid bulk in solid-body rotation. Owing to its importance for the present study we treat the oscillating Ekman layer in more detail here (see also Greenspan 1969; Busse *et al.* 2007). We refer to an Ekman layer as oscillating when it forms over a librating surface (with respect to the corotating frame). A librating surface at an angle $\alpha \neq 0$ to the rotational axis periodically generates vorticity. This appears to be a more general feature of any inclined wall, wherefore we use this formulation in favour of the velocity.

First, (5.1) are cross-differentiated and new variables are introduced: the local wall-normal vorticity $\zeta' = \partial v'/\partial x' - \partial u'/\partial y'$ and the local wall-tangential divergence $D' \equiv \boldsymbol{\nabla}_{\parallel} \cdot \boldsymbol{v}' = \partial u'/\partial x' + \partial v'/\partial y'$. The boundary-layer approximation (5.1) yields

$$\frac{\partial D'}{\partial t} - f_* \zeta' = E \frac{\partial^2 D'}{\partial z'^2}, \quad \frac{\partial \zeta'}{\partial t} + f_* D' = E \frac{\partial^2 \zeta'}{\partial z'^2}, \tag{5.4a,b}$$

which is completed by the boundary conditions $\zeta' = \varepsilon f_* \sin \omega t$ and $D' = 0$ at $z' = 0$. Regularity requires $D', \zeta' \to 0$ for $z' \to +\infty$. Separation of variables yields the ansatz $\zeta' = X_1 \sin \omega t + X_2 \cos \omega t$ and $D' = Y_1 \sin \omega t + Y_2 \cos \omega t$ for real-valued amplitudes. Equations (5.4) are solved by standard procedure by collecting the amplitudes in complex variables $W \equiv X_1 + \mathrm{i}Y_1$ and $Z \equiv X_2 + \mathrm{i}Y_2$. From a straightforward calculation one obtains

$$\hat{L}W = -\omega Z, \quad \hat{L}Z = +\omega W \quad \text{with } \hat{L} \equiv \left[E \frac{\partial^2}{\partial z'^2} + \mathrm{i}f_*\right]. \tag{5.5a,b}$$

The general solution for W reads (regularity $|W| < +\infty$ implied)

$$W \equiv X_1 + \mathrm{i}Y_1 = C_1 \mathrm{e}^{(\mathrm{i}s-1)z'/\delta'_-} + C_2 \mathrm{e}^{(\mathrm{i}-1)z'/\delta'_+}, \tag{5.6}$$

where $s = \mathrm{sgn}(f_* - \omega)$ is the sign function and $\delta'_\pm = \sqrt{2\nu/|f_* \pm \omega|}$ are the oscillating Ekman layer depths with $\delta'_- \geqslant \delta'_+$ (see figure 10; solid and dashed lines with bars and crosses). Both layers together adjust the boundary condition to the bulk flow. Only the layer δ'_- erupts for $\omega \to f_*$ from either side of the singularity. On a librating lid it is $\alpha = \pm\pi/2$ and $|f_*| = f$, which makes $\delta'_\pm = \delta_\pm$. This corresponds to the case considered by Busse *et al.* (2007). The Ekman layers $\delta_\pm$ (on a lid) and $\delta'_\pm$ (on the frustum)

have in common that they approach constant values in the limit $\omega \to 0$, which are the classical Ekman layer depths on the f-plane.

Note that boundary conditions to (5.6) yield real-valued constants $C_1 = C_2 = \varepsilon f_*/2$. Then Z can be computed from W, so that D' and ζ' can finally be obtained. Exploiting axisymmetry, $\partial(\cdot)/\partial x' = 0$, the velocity field can be computed (see also appendix D). The full solution is not of interest here. Instead, let us focus on another aspect: the divergence-free condition for the velocity field yields the existence of a homogeneous wall-normal influx into the boundary layer that balances the wall-parallel Ekman flux. The influx velocity w'_E on top of the boundary layer, the so-called Ekman pumping/suction velocity (depending on the librational phase), is strictly vertical (see Busse *et al.* 2007). It can be obtained by integrating the continuity equation, $D' = -\partial w'/\partial z'$, along the stretched coordinate $\xi = z'/\delta_{BL}$. By making use of impermeability $w'|_{z'=0} = 0$ we get

$$w'_E = -\delta_{BL} \int_0^{+\infty} D' \,\mathrm{d}\xi = -\frac{\varepsilon \nu^{1/2}}{\sqrt{2}} \sin(\omega t - \chi) \times \begin{cases} f_*^{3/2}/\sqrt{f_*^2 - \omega^2} & \text{for } \omega < f_* \\ f_* \sqrt{\omega - \sqrt{\omega^2 - f_*^2}}/\sqrt{\omega^2 - f_*^2} & \text{for } \omega > f_* \end{cases} \tag{5.7}$$

with the phase shift χ given by

$$\sin\chi = \frac{-\left(\delta'_- - \delta'_+\right)}{\sqrt{\left(s\delta'_- + \delta'_+\right)^2 + \left(\delta'_- - \delta'_+\right)^2}} = \begin{cases} -F(\omega/f_*)/2 & \text{for } \omega < f_*, \\ -1/\sqrt{2} & \text{for } \omega > f_*. \end{cases} \tag{5.8}$$

For $\omega < f_*$ the phase term $\sin\chi(\omega)$ has a dependency on $F(\omega/f_*)$, which is given in (D 5). The phase term $\sin\chi(\omega)$ monotonically decreases from 0 to $-1/\sqrt{2}$ at $\omega = f_*$, where the derivative has a singularity. For $\omega > f_*$ the phase shift is a constant corresponding to $\chi = -\pi/4$. Interestingly, $w'_E(\omega)$ reaches a constant amplitude $\varepsilon\sqrt{2\nu f_*}/2$ in the limit $\omega \ll f_*$, whereas it tends to zero in the high-frequency limit $\omega \gg f_*$. Lastly, w'_E increases infinitely for $\omega \to f_*$ due to the boundary layer eruption. More precisely, Maas & van Haren (1987) showed that in this case a z'^2-profile of velocity will be established. The functional behaviour of $w'_E(\omega)$ is generally quite similar to $\delta'_-(\omega)$ (see figure 10). Note that the same features are present also for a librating lid by formally replacing $f_* \to f$ and $\delta'_- \to \delta_-$.

Following Busse *et al.* (2007) the 'horizontal' flux divergence $\boldsymbol{\nabla}_\parallel \cdot \boldsymbol{Q} = \partial Q'_x/\partial x' + \partial Q'_y/\partial y'$ exhibited by an oscillating Ekman layer is coupled to the Ekman pumping velocity w'_E. The associated mass flux balance reads

$$w'_E = -\delta_{BL} \int_0^{+\infty} D' \,\mathrm{d}\xi = -\boldsymbol{\nabla}_\parallel \cdot \boldsymbol{Q}. \tag{5.9}$$

By $f_* = f \sin\alpha$ in w'_E the inclination angle α directly affects the ('horizontal') flux $\boldsymbol{Q}$ and its dependency on the forcing frequency ω.

In contrast to the Ekman layer, a Stokes layer over the librating outer cylinder only carries an oscillating azimuthal flux. Due to finite height, the Stokes layer induces secondary Ekman layers within the interaction regions near the corners C and D, which are radial–axial patches of the order $\delta_S \times \delta_-$. The induced Ekman layer on one of the lids exhibits a flux deficit with respect to the geostrophic flow on top of

it (cf. Busse *et al.* 2007). The mathematical treatment of the flux deficit is similar to the Ekman flux $\boldsymbol{Q}$ outlined above. In case the lids librate together with the outer wall, the boundary-layer interaction becomes more distinct. Qualitative arguments are then no longer sufficient and a detailed analysis of the corner flow problem would be required. We will make use of the boundary layer and the mass flux (deficit) to understand the localization of wave excitation which we discuss in the following section.

5.2. *Excitation mechanism*

Under the presence of boundary layers we quantify wave excitation by distinguishing: (i) coupling of wall libration and boundary layer and (ii) coupling of boundary layers and bulk flow. We assume that waves excited in the bulk are of substantially smaller amplitude than the oscillating boundary layer in accordance with observations in § 4. The oscillatory boundary layer (frequency ω) thus provides the primary flow due to which waves will be excited. We also assume that classical boundary layers are approximately realized locally. Then, with respect to (i), we shall see to which degree classical boundary-layer theory is useful to understand the cavity flow excited. Regarding (ii) we note that wave excitation mechanism refers to the mechanics in the fluid rather than libration (even though they are not unrelated). It is due to the dominance of the wave beams excited in the corners of the trapezoid ABCD that we focus our attention on this mechanism.

We can consider wave excitation as linear process due to dominance of the signal at the forcing frequency ω and its persistence for $\varepsilon \ll 1$. The reason appears to be a mass flux discrepancy in the primary flow emerging at a corner. More precisely, it is a mismatch in the local wall-tangential fluxes Q'_y and thus a mismatch of the Ekman pumping w'_E (see 5.9) in the two overlapping boundary layers. This is shown for the corners A and D in figure 11 for simulation results (see also figure 3(*b*), where the situation Q'_y, $Q'^{(2)}_y < 0$ is sketched corresponding to the prograde phase of libration). Interestingly, only for the frustum libration (figure 11*a*, solid line) an anharmonic behaviour is strongly visible. This indicates presence of nonlinearity in the boundary layer, which enhances the flux discrepancy. If ε is reduced to $O(10^{-2})$, all curves become sinusoidal, but a discrepancy in the fluxes is preserved. The anharmonic content vanishing for $\varepsilon \ll 1$ is thus consistent with the simultaneous disappearance of the azimuthal mean flow layer (cf. figure 6*c*) due to reaching the linear regime. Note also that we selected $\omega = 0.47$ in figure 11 to ensure that no wave beam is incident to the corners.

From the above reasoning we can infer that a homogeneous influx of fluid into the frustum boundary layer due to Ekman pumping/suction must be balanced by a localized outflow from the boundary-layer interaction volume in the vicinity of corner A (and B). This jet-like outflow, seen in the (r, z)-plane, is directed roughly along the bisectrix of the corner due to geometric constraints. Numerical simulations reveal a rather rich kinematic behaviour that breaks symmetry of the pumping/suction process of the emerging jet and is beyond the qualitative argumentation. Note in this regard that the Ekman flux $\boldsymbol{Q}$ also has an azimuthal component whose role is not quite clear. In any case, it is the frequency ω of the forcing that fixes possible directions of wave beams excited locally. Once excited, the waves carry momentum and kinetic energy from the boundary layers into the fluid's bulk.

The whole argument can also be applied to the case of lids plus outer cylinder libration, where oscillating and passive Ekman layers are present at corners A and

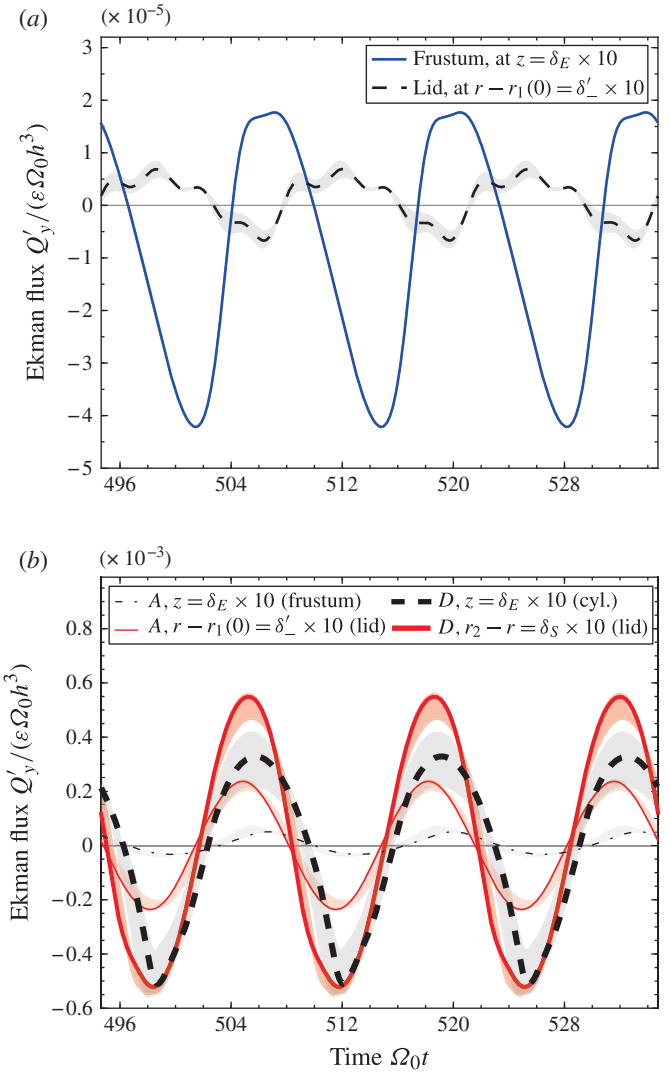

FIGURE 11. (Colour online) Wall-tangential mass flux in the boundary layer for three libration periods for the stationary regime: (*a*) $\omega = 0.47$, $E = 1.3 \times 10^{-6}$, $\varepsilon_{num} = 0.2$; (*b*) $\omega = 0.47$, $E = 1.3 \times 10^{-6}$, $\varepsilon_{num} = 0.1$. The component $Q'_y(t)$ lies in the (r, z)-plane according to the local coordinates defined in figure 1(*b*). Fluxes in the vicinity of corner A for the frustum in libration are shown in (*a*), those near corners A and D for outer cylinder and lids in libration are shown in (*b*). Locations are at roughly $10 \times \delta_{BL}$ (cf. figure 10) away from the corner in the r or z direction, respectively. Integration was done over $3(\pm 1) \times \delta_{BL}$. The shading indicates the confidence interval due to variations of integration length and location.

B (with primary and induced layers from above exchanged). In addition, oscillating Ekman and Stokes layers interact at corners C and D. As mentioned earlier, this problem seems more involved. It is worth noting that libration of the outer cylinder alone can hardly excite waves. This is because, to first order, a wall-parallel flux

towards the corners is absent. Only secondary Ekman layers on the lids could then excite waves, which is supported also by numerical results for lid libration alone (not shown here). In the next section we focus on the frequency dependency and the possible interrelation between boundary layer and bulk flow.

5.3. *Subdomain analysis*

We investigated the coupling between oscillating boundary layers and bulk flow in order to quantify wave excitation in the bulk (by corner beams) as was observed and simulated. Our hypothesis consists of three parts: (i) formation of an oscillating Ekman layer that drives a wall-parallel Ekman flux $\boldsymbol{Q}$; (ii) the deflection of that flux in the corners due to $\boldsymbol{Q}$-discrepancy; and (iii) local excitation of inertial waves meeting the dispersion relation locally.

The flux balance (5.9) suggests that $\boldsymbol{Q}$ scales with the Ekman pumping velocity w'_E as a consequence of mass conservation (2.3). Following the qualitative arguments, we expect velocity amplitudes of the waves excited to scale with the flux discrepancy near a corner in the boundary layer. The latter would thus be related to the Ekman pumping, for which we have an estimate given by (5.7). This can be exploited by investigating the frequency dependence of the flow. From measurements and simulations it is known that a global trend is visible in excited wave amplitudes that is qualitatively similar to the boundary-layer eruptions seen in figure 10 when the libration frequency is varied. Besides that, resonant excitation of inertial waves was observed for certain frequencies as we shall see below.

Five subdomains were defined (shaded areas in figure 3) and, for simplicity, all of them were kept fixed over the range of forcing frequencies investigated (we will come back to the robustness further down). Corner regions corresponding to the heights of neighbouring subdomains were excluded to avoid overlap (see the enlarged views in figure 3). Boundary-layer domains were chosen such that they initially covered only a few δ_E in axial and δ'_E in radial direction (cf. figure 10). From there on, the extent was increased until tens of boundary-layer depths were covered. A similar approach was taken by Sauret *et al.* (2012). In general, it is the scale separation between boundary layer and bulk flow (cf. § 4) ensuring that the bulk flow portion captured by the boundary-layer domain is approximately negligible. We found that the frequency dependence shown in figures 12–14 is independent of the precise thickness of the boundary-layer domain as long as boundary layer and bulk are well-separated.

In the following we consider the dominant signal oscillating with the forcing frequency ω. As a measure of flow activity we calculated total kinetic energy K_ω from frequency-filtered velocities $\boldsymbol{v}_\omega$, i.e.

$$K^i_\omega \equiv \int_{V_i} \frac{\boldsymbol{v}^2_\omega}{2}\,\mathrm{d}V, \tag{5.10}$$

where V_i denotes the volume of subdomain i according to figure 3. In the bulk, K^{bulk}_ω measures the energy of propagating waves (other oscillatory large-scale flows are not visible). The frequency filter used is described in appendix C.

5.3.1. *Frustum libration*

The frustum features only a single modulation frequency, determined by the half-apex angle α, for which we expect the boundary layer to erupt all along the boundary (cf. the thick (blue online) solid line in figure 10). This is in contrast to spherical

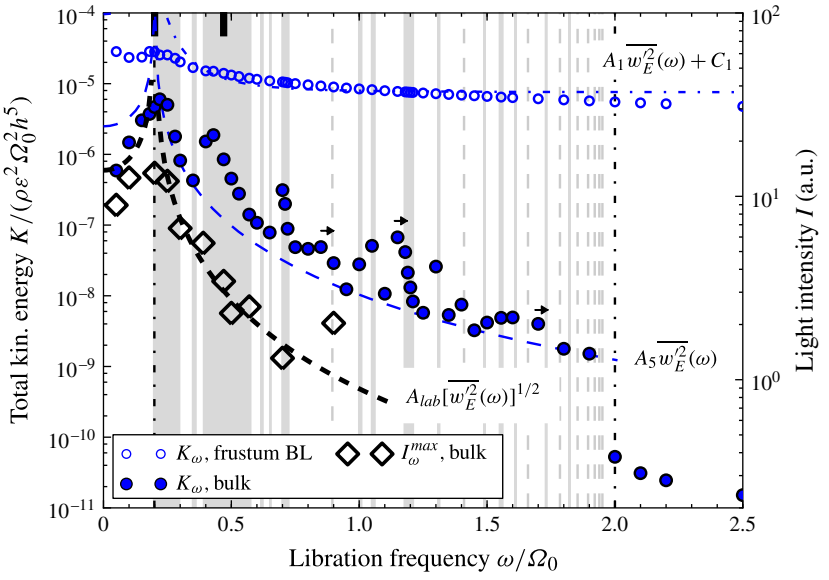

FIGURE 12. (Colour online) Wave excitation by frustum libration for filtered quantities. Total kinetic energy K_ω^i in the subdomains $i = 1, 5$ according to figure 3(*a*) from the numerical simulations and maximum light intensity I_ω^{max} measured in the bulk part of a meridional slice ($\varphi = \text{const.}$). Thick bars on the upper axis indicate the cases shown in § 4. Fixed parameters are $E = 1.3 \times 10^{-6}$ and $\varepsilon = 0.2$. Fitted coefficients are $A_{lab} = 7.71 \times 10^4$, $A_1 = 1.37 \times 10^3$, $A_5 = 38.5$, $C_1 = 7.60 \times 10^{-6}$. See the text for details.

shells, where all inclination angles $-\pi/2 \leqslant \alpha \leqslant \pi/2$ are present and one always finds a latitude at which the Ekman layer erupts (e.g. Kerswell 1995).

The qualitative argumentation outlined in § 5.2 can be applied as follows. Equation (5.9) has already been integrated over the whole boundary-layer height. The total kinetic energy of the oscillating Ekman layer thus reads $K_\omega^E \propto \hat{w}_E'^2(\omega)$, where $\hat{w}_E'$ denotes the oscillation amplitude found in (5.7). Due to the sinusoidal time dependence it can be computed (modulo a factor of 2) by taking the temporal average over one libration period of the squared velocity, i.e. $\hat{w}_E'^2 = 2\overline{w_E'^2}$. The interior wave field should then possess the same frequency dependence as the oscillating Ekman layer. The expected scalings are shown in figure 12 as fits (dashed lines with the same colour as the data).

Figure 12 shows the simulated total kinetic energy (K_ω, left scale, blue online) as function of the forcing frequency ω in the subdomains bulk ($i = 5$; according to figure 3*a*) and frustum boundary layer ($i = 1$). Also shown is the frequency-filtered light intensity measured in the laboratory (I_ω^{max}, right scale, black). Flow fields presented in § 4 correspond to the frequencies marked by thick bars at the upper axis of figure 12. Dash-dotted vertical lines indicate the frustum boundary layer eruption ($\omega = 0.2$) and the limit of the inertial wave band ($\omega = 2$). Grey vertical patches illustrate low-order wave attractor windows obtained by ray tracing (see also figure 4). Dashed grey lines show frequencies of periodic orbits, which become denser as $\omega \to 2$. A mean frequency resolution of $\Delta\omega = 0.05$ could be realized, coarser for the higher frequencies (less important due to reduced excitation efficiency) and finer in low-order wave attractor windows. Cases for $\omega > 2$ are shown as well, for which no wave excitation in the linear limit is expected.

Filtered light intensities were truncated by a spatial maximum norm to yield a single point per measurement. Note that the curve of I_ω would be less pronounced but similar if a spatial average would have been used. Optical measurements provide data for the bulk only. Following the qualitative arguments from above, velocity amplitudes in the wave field are expected to scale with the Ekman pumping velocity. The frequency dependence of the visualized shear is proportional to that of velocity (black dashed curve). Hence, we expect a correlation to the amplitude $\hat{w}'_E(\omega)$ on the right-hand side of (5.7). One should not over-interpret the frequency dependence of the measurements due to different (optical) errors. For $\omega = 0.7(0.8)$, for instance, it is not clear whether the measured values are artificially reduced (enhanced). The least we can say is that for $\omega \gtrsim 0.6$ waves are not excited efficiently and shear associated with the waves is too small to orient the particles sufficiently, so that the signal-to-noise ratio in I_ω^{max} is too large for a reliable analysis. Nevertheless, a clear tendency is visible for $0.1 \leqslant \omega \leqslant 0.5$ pointing to the boundary-layer eruption at $\omega = f_* = 0.2$.

In figure 12 qualitative agreement is found for the bulk flow between measurements (diamonds) and simulations (filled circles). The bulk kinetic energy reaches a maximum at the eruption frequency close to $\omega = 0.2$. Applying the qualitative argumentation (Ekman flux discrepancy in the corners A and B), we can infer that kinetic energy of the waves excited has to scale with respect to ω as the squared amplitude of the Ekman pumping, say $K_\omega^{bulk} \propto \overline{w_E'^2}(\omega)$. This is nicely seen in the non-resonantly excited waves, for which K_ω^{bulk} follows the dashed (blue online) line, except for distinct local maxima (resonance peaks). All of them are located in wave attractor windows obtained by ray tracing ($\omega = 0.25, 0.35, 0.7, 1.05, 1.17, 1.3$). Only the less pronounced peaks at $\omega = 0.85$ and 1.4 correspond to periodic orbits. The small arrows (here only pointing to the right) indicate that the interior wave field exhibits the spatial structure of a ray tracing path with a frequency roughly at the tip of the arrow. A similar shift in frequency between ray tracing and eigenfrequencies has recently been described by Lopez & Marques (2014). They argue that the wave beams are not emitted exactly at the corners and are not reflected at the walls but within the boundary layers. Thus, the domain in which the waves propagate does not exactly match with the geometry considered.

An interesting feature is the asymmetry of resonance peaks within wave attractor windows (e.g. the intervals around $\omega = 0.4, 0.7, 1.2$). This can be understood in terms of the localization of the forcing at corners A and B, the radial dependency of the wall velocity $v_{w,\varphi}(r)$ (where $r_1(0)/r_1(h) = 2$) and the path length needed until a wave beam is practically focused. In a viscous medium the damping length is finite (see Phillips 1963) and we expect a resonance to decrease with increasing distance a wave packet has to travel until it reaches the wave attractor. Looking at figures 5 and 7(*a*), for instance, we see that the stronger beam from A ($\omega = 0.2$) is fed onto the wave attractor, while the other beam from corner B is damped before reaching it. This is reversed for $\omega = 0.296$ and is similar for the other wave attractor windows. Across the window at $\omega \approx 1.2$ the general frequency dependence of the forcing can be neglected. Assuming that damping is similar for the modes excited at $\omega = 1.18$ and 1.21, we would expect kinetic energy to reduce roughly by an order of magnitude due to the radial dependence of the wall velocity. This corresponds qualitatively to figure 12. Shifts of the local maxima towards the centre of wave attractor windows may be due to modified geometry (boundary layers, slope transitions) and interference of wave beams in case of the wave attractors for the limiting frequencies. Here the resolution $\Delta\omega$ seems not yet sufficient to clarify this.

In figure 12 we can also see that the boundary-layer domain shows agreement with boundary-layer theory. We fitted a generic function (dash-dotted line) that consists of a term proportional to the Ekman pumping and a constant offset C_1 due to libration (this is the evanescent part not present in the bulk). This is certainly a rather empirical approach, but covers the behaviour inside the inertial wave band quite well. For the oscillating boundary layer, Ekman pumping is notable only near the eruption frequency f_*, where the otherwise constant value is increased by a factor of 3.

All fits (dashed and dash-dotted lines) were obtained for $\omega > f_*$ where we have the majority of data points. Note that to the left of the peak ($\omega < f_*$) values predicted by the scalings are only about twice as large as those simulated and observed. This is acceptable considering the heuristic argumentation used for derivation of the frequency dependence, as well as the simplifications made in the boundary-layer analysis and the domain decomposition.

The interval $\omega \lesssim E^{1/2}$ has to be excluded due to spin-up (e.g. Smirnov *et al.* 2005). On the other hand, inertial instabilities become more important for $\omega \to 0$ (e.g. Koch *et al.* 2013). For $\varepsilon = O(10^{-1})$ and $E = O(10^{-6})$ boundary-layer instabilities occur before any notable spin-up effects. Small-scale vortices develop first in the corner A during the prograde phase of libration and spread upward along the frustum wall if ε is increased or ω is reduced. Then wave excitation can no longer be considered as a completely linear process. Instead it is replaced gradually by spontaneous emission of inertial waves (Sauret *et al.* 2012, 2013). With notable nonlinearity, energy can be extracted from the forcing frequency ω and thus shift the system response to other frequencies in the spectrum. From numerical simulations for $\varepsilon_{num} = 0.2$ and $E = 1.3 \times 10^{-6}$, the onset of boundary-layer turbulence was notable for forcing frequencies $\omega \lesssim 0.2$. In this range K_ω^{BL} in the frustum boundary layer can also suffer from aliasing (coarse temporal resolution of time slices used for filtering) and violation of stationarity.

Also visible in figure 12 is that K_ω of the bulk is much smaller than that of the frustum boundary layer, except for boundary-layer eruption. We neglected wave–boundary-layer interaction, but from the local solutions (bulk flow over a wall) an additional loss of kinetic energy can generally be expected for a wave beam impinging on a wall. Note that there are no resonance peaks visible in the corresponding boundary-layer curve K_ω^{BL} shown in figure 12. Thus, the waves are present in the bulk, but they do not effect much the boundary layer dynamics. Boundary-layer theory developed in § 5.1 seems to be an acceptable approximation also in the wave regime. The reason might be the limited power influx by libration (cf. appendix D) and geometry, i.e. $\alpha \ll 1$. For larger apex angles and non-axisymmetric forcing boundary layer theory might no longer work. Integral quantities of the boundary-layer analysis change quantitatively but not qualitatively if the domain decomposition is varied. The points close to $\omega = 0$ and 2 are those most affected. Hence also the drop of K_ω^{bulk} at $\omega = 2$ changes in magnitude. However, we found the signals qualitatively robust once this drop was substantial (one order of magnitude or higher). For the selected decomposition (see also table 1) we can say that the error level is $\Delta K_\omega^{bulk} \approx 5 \times 10^{-11}$ as can be seen from the points in the range $\omega > 2$.

5.3.2. *Lids plus outer cylinder libration*

In case of lids and outer cylinder in libration no singularity is present within the inertial wave band $(0, f)$. However, Stokes and Ekman layer eruptions occur at $\omega = 0$ and $\omega = f$, respectively (non-dimensional Coriolis parameter $f = 2$).

	$(\Delta N_r, \Delta N_z)$	$A \times 10^{-7}$	a	$B \times 10^{-7}$	b	$B' \times 10^{-5}$	b'
	(12, 6)	8.56	1.058	0.87	0.923	2.20	1.149
	(24, 12)	4.48	1.037	1.46	0.996	1.43	1.317
	(32, 16)	3.26	1.029	2.08	1.043	2.03	1.364
	(40, 20)	2.29	1.021	2.72	1.087	2.59	1.406
*	(48, 24)	1.55	1.014	3.18	1.126	2.85	1.440
	(52, 28)	1.25	1.011	3.05	1.138	2.70	1.452
	(56, 48)	1.06	1.010	1.94	1.122	2.15	1.452

TABLE 1. Fit coefficients for the energy ratio $K_\omega^{bulk}/K_\omega^{BL}$ using different domain decompositions. The decompositions are identified by the number of grid cells trimmed from the bulk along each wall in radial and axial direction $(\Delta N_r, \Delta N_z)$. Unprimed variables B, b are for the fits excluding the strongest two resonances $\omega \approx 0.9, 1.40$ for the lids and outer cylinder libration case. The asterisk (*) marks the domain decomposition used for figures 12–14.

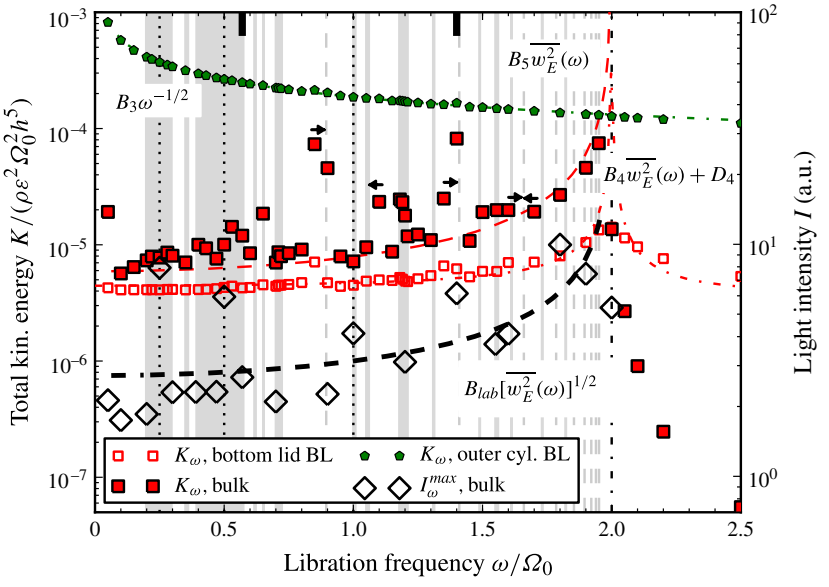

FIGURE 13. (Colour online) Wave excitation by libration of the lids together with the outer cylinder for filtered quantities. Total kinetic energy K_ω^i in the subdomains $i = 3, 4, 5$ according to figure 3(*a*) from the numerical simulations and maximum light intensity I_ω^{max} measured in the bulk part of a meridional slice ($\varphi = \text{const.}$). Thick bars on the upper axis indicate the cases shown in § 4. Fixed parameters are $E = 1.3 \times 10^{-6}$ and $\varepsilon_{lab} = 0.2$ and $\varepsilon_{num} = 0.1$. Fitted coefficients are $B_{lab} = 4.77 \times 10^3$, $B_3 = 0.164$, $B_4 = 1.14$, $B_5 = 9.11$, $C_4 = 3.70 \times 10^{-6}$. See the text for details.

Figure 13 shows total kinetic energy (K_ω, left scale, red online) as a function of the forcing frequency ω in the subdomains bulk ($i = 5$ according to figure 3*a*) and the boundary layer over the librating walls ($i = 3, 4$). Also shown is the frequency-filtered light intensity measured in the laboratory (I_ω^{max}, right scale, black). Top and bottom lids behave almost identically, wherefore we skipped the plot for the top lid Ekman layer ($i = 2$) in the kinetic energies. The underlying vertical patches and lines are the same

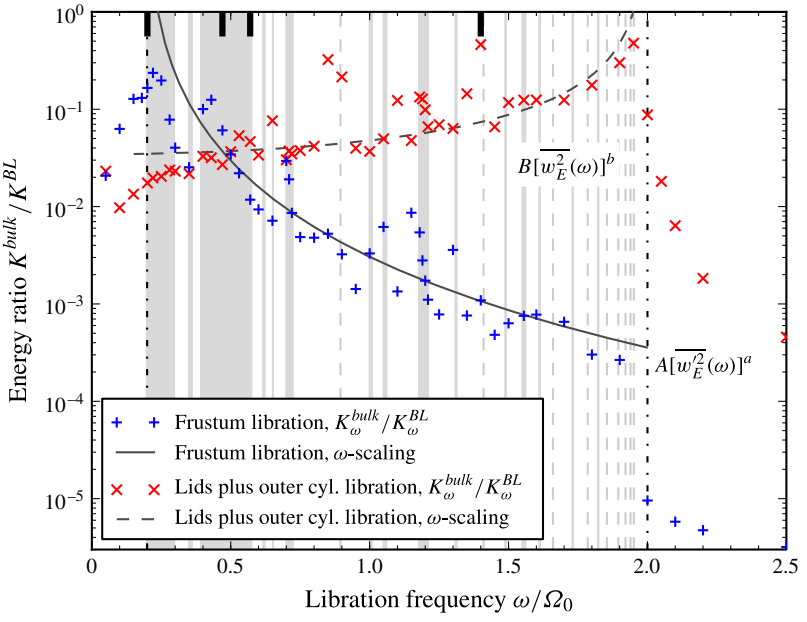

FIGURE 14. (Colour online) Wave excitation efficiency given by the energy ratio $K_\omega^{bulk}/K_\omega^{BL}$ for two different configurations (frustum libration with pluses (blue online); lids and outer cylinder libration with crosses (red online)). The quotient was computed from simulated total kinetic energies shown before. K_ω^{BL} is the sum over all oscillating boundary layers. Fits (dashed and solid black lines) were obtained by a least-squares fit of the data sets. See the text and table 1 for details.

as in figure 12 and indicates low-order wave attractors and periodic orbits obtained by ray tracing (cf. figure 4). Thick bars on the top axis indicate the results discussed for this configuration in § 4. To each data set the expected frequency dependence (see (5.7) and the Stokes layer scaling) has been plotted by dashed and dash-dotted lines of corresponding color.

The highest energy component in figure 13 is the Stokes layer's total kinetic energy (pentagons). It exhibits only an azimuthal velocity component according to the boundary layer analysis. Considering the aspect ratio $\Delta r(0)/h = 1/5$, the kinetic energy density in the Stokes layer is practically given by the local solution, i.e. $v_\omega^2/2 = U^2/2$ and $U = \varepsilon r_2$. Integration over the Stokes layer yields the estimate $K_\omega^S \approx \pi U^2 \delta_S(\omega) \propto \omega^{-1/2}$. Indeed, the Stokes layer's frequency dependence shown in figure 13 is practically perfect. Surprisingly, this holds in the low frequency limit as well. This means that even though nonlinear phenomena appear for $\omega \to 0$ (as discussed for the frustum libration case) they are of much smaller kinetic energy than the underlying azimuthal flow induced by the librating wall. As a secondary phenomenon at the outer wall, Taylor–Görtler vortices form along the outer cylinder similar to the full cylinder (see Sauret *et al.* 2012).

In figure 13 qualitative agreement can be seen for the bulk flow between simulations and measurements. A constant value is approached in the waves' kinetic energy as $\omega \to 0$, which is consistent with the theoretical prediction of w_E (see (5.7); note that unprimed variables for the lid are obtained by formally replacing $w_E' \to w_E$ and $f_* \to f$). Wave energy increases for $\omega \to f$ and is followed by a sharp drop as $\omega \geqslant f = 2$.

This drop appears stronger than in figure 12 because boundary layer eruption of the lid's oscillating Ekman layer coincides with wave band limit f. We also observe the proportionality to Ekman pumping velocity (for measured I_ω^{max}) or its square (for the simulated kinetic energy K_ω^{bulk}) as indicated by the fitted functions.

Non-monotonic behaviour of the data K_ω in figure 13 can be attributed to resonance. Similar as for the frustum libration, low-order patterns accumulate energy in the wave field. These do not necessarily correspond to wave attractors as can be seen when inspecting the shaded areas. We found strong peaks with spatial structures corresponding to periodic orbits (dashed vertical grey lines), e.g. $\omega \approx 0.9, 1.4$. The peaks at $\omega \approx 0.9, 1.4$ were excluded in the fits (dashed and dash-dotted lines, red online) in order to have the data compliant with approximately non-resonant wave excitation (cf. §§ 5.1 and 5.2). The pattern for $\omega = 1.4$ is shown in figure 9. A larger peak, however, occurs in the simulations at $\omega \approx 0.9$. More precisely, for a shifted frequency $\omega = 0.85$ (indicated by an arrow). In the ray picture the modes have a tilted V- and W-shape. The outer as well as the inner corners are connected and waves are therefore directly emitted onto the periodic orbits. This is a geometric interpretation for resonant behaviour found in figure 13. The frequency $\omega = 1.66$ might be quasi-resonantly excited by the libration frequencies $\omega = 1.6$ and 1.7 as indicated by two opposed arrows. For the attractor windows we find a significant peak at $\omega \approx 0.62, 1.2$, but only a weak signal for $\omega \approx 0.25, 0.5$. As $\omega \to 2$, the 'spectrum' gets denser and spatial patterns show more reflections, which makes identification difficult. However, the few data points at $\omega = 1.85, 1.9, 1.95$ show spatial patterns corresponding to periodic orbits of ray tracing solutions (consisting of several 'tilted Vs' similarly to figure 9).

The periodic orbits correspond to modes that exist for one frequency only. When they are excited quasi-resonantly this gives an idea of 'line broadening' in the spectrum due to viscosity. Considering the two frequencies $\omega = 0.9, 1.4$ we can say that the line broadening is of the order of $\delta\omega \approx 0.05$, which is the resolution along the ω-axis for the simulations carried out. We attribute the line broadening to boundary layers, wave beams of finite-width and modification of geometry next to corners A and B. The peak at $\omega = 0.85$, for instance, shows a V-like pattern connecting A and B, whereas that at $\omega = 0.9$ is dominated by the mirrored one connecting corners C and D.

The oscillating Ekman layer over the lid (unfilled squares (red online) in figure 13) exhibits good agreement with the boundary-layer theory but shows only traces of the bulk flow resonances. This justifies the boundary-layer analysis and domain decomposition also for the lids and outer cylinder in libration, even though the kinetic energy of the bulk is now larger than that over the lid.

Measurements I_ω^{max} in figure 13 show the same trend to higher energies across the inertial wave band as ω increases. One series of peaks does not coincide with those seen in simulations: $\omega = 0.25, 0.5, 1.0$. This can be attributed to imperfections of the experimental set-up in combination with the frequency filter used. Libration of the imperfect outer cylinder results in a frequency modulated optical signal. If the (filter) frequency ω is an integer fraction of the mean rotation rate $\Omega_0 = 1$, the comb of frequencies coincides with the sideband spectrum of the frequency-modulated signal recorded by the camera. As a result, the harmonic analysis samples optical artifacts. These are originating from the shape of the glass cylinder, an inhomogeneous particle distribution and particles sticking to the wall, resulting in an artificial increase of measured light intensities for frequencies $n\omega \leqslant f$ (where $n = 0, 1, 2, \ldots$). We highlight the frequencies affected by optical artifacts by dotted vertical lines in figure 13

($\omega = 0.25, 0.5, 1.0$). In this regard we may only note that an off-centre mount on the turntable and elliptical deformation (manufacturing tolerances) have the largest impact, since they yield the smallest possible carrier frequencies $\Omega_c = 1, 2$ that fall into the inertial wave band.

The driving flow in the case of lids plus outer cylinder libration is given by (i) oscillating Ekman layers over the lids and (ii) Stokes layer over the outer cylinder. In the linear limit, the situation is close to libration of the lids alone. Figure 13 shows that the oscillating Ekman layers over the librating lids are correlated with the wave energy in the bulk, which is in agreement with the theoretical arguments. This is similar to results on libration-induced flows for a full cylinder in an asymptotic limit of small libration frequencies (Wang 1970; Busse 2010) in which outer cylinder libration has been neglected. Nevertheless, the Stokes layer over the librating outer cylinder is not negligible *per se*. Its effect might be more subtle by modifying the corner flow problem and inducing a jet-like mean flow close to the wall by streaming.

5.3.3. *Wave excitation efficiency*

Wave excitation efficiency is discussed in the following by investigating energy input by librating walls, energy in the boundary layers and energy in the bulk. As shown in appendix D, spectral power input by libration is connected to the oscillating boundary layer over librating walls. The wave field's energy K_ω^{bulk} is a result of the balance of energy input, nonlinearity and viscous dissipation. No theory exists for the frequency dependence of wave energy in the bulk, wherefore we investigate it empirically by considering the coupling of boundary layer and bulk flow.

We consider the energy ratio $K_\omega^{bulk}/K_\omega^{BL}$ as measure for wave excitation efficiency, where K_ω^{BL} denotes the sum of K_ω^i over all oscillating boundary layers i according to figure 3(a). This is based on the assumption that the oscillating boundary layer provides the primary flow which is (partly) transformed into waves. Frequency-filtering ensures that we compare only data possessing the same time scales, here ω^{-1}. The energy ratio makes it possible to compare the two different configurations more directly in terms of energy input by libration versus energy of inertial waves excited.

Figure 14 shows the simulated wave excitation efficiency as a function of the libration frequency ω in the inertial wave regime ($0 < \omega < f = 2$). The shaded vertical structures are the same as in figures 12 and 13. Small thick bars on the upper axis indicate frequencies selected for cases shown in § 4. Two clear trends are obvious: (i) frustum libration is generally most efficient at the Ekman layer eruption $\omega = f_* = 0.2$, decreasing to the left and right; (ii) lids and outer cylinder in libration excites waves more efficiently as $\omega \to f = 2$. Both data sets, corresponding to the two configurations investigated, exhibit pronounced fluctuations around the fitted curves. These are due to resonance at low-order wave attractor and periodic orbit frequencies.

The non-resonant behaviour of $K_\omega^{bulk}/K_\omega^{BL}$ can be understood by qualitative arguments. The oscillating boundary layer is of roughly constant kinetic energy (far from the eruption frequency). Thus, $K_\omega^{bulk}/K_\omega^{BL}$ can be fitted to the squared Ekman pumping amplitude. In the ansatz functions the pole of the respective Ekman layer eruption is preserved (see (5.7)), but we allow for a change in the scaling exponent. Table 1 collects the coefficients obtained by a least-squares fit in the frequency interval $0.25 < \omega < 1.95$ for different domain decompositions and the two configurations investigated. Results in figures 12–14 are corresponding to the decomposition marked with an asterisk (*). On the one hand, for the case of frustum libration (coefficients A, a) and lids plus outer cylinder libration (coefficients B', b') all points in the range have been used. On the other hand, for the case of lids

and outer cylinder libration, the coefficients B, b correspond to a fit excluding the strongest two resonance peaks at $\omega = 0.90 \pm 0.05$ and $\omega = 1.40 \pm 0.05$. In figure 14 we show the fits corresponding to A, a and B, b (similarly to the fits in figures 12 and 13). Inspecting the spectra corresponding to the decompositions (not shown here), we can consider the decompositions (32, 16)–(52, 28) as geometrically acceptable. Decomposition (56, 48) suffers from a too small bulk portion. Averaging over the decompositions (32, 16)–(52, 28) yields

$$a = 1.02 \pm 0.01, \quad b = 1.09 \pm 0.05, \quad b' = 1.41 \pm 0.05. \tag{5.11a–c}$$

The exponents a and b are close to one, as one would expect for the case without resonant excitation of eigenmodes. In this sense, the frustum libration case behaves much simpler than the lids and outer cylinder libration case. In the latter, b' is close to $3/2$, indicating a strong effect of resonant wave excitation not captured by our theory. The prefactors A, B, B' are just proportionality constants that depend also on the exponents (see the magnitudes of B and B' in table 1). The non-monotonic variation of B and B' with the decomposition appears because the size of the excluded regions increases with the number of grid cells trimmed from the bulk, i.e. ΔN_r in radial and ΔN_z in axial direction (cf. figure 3). Note further that the coefficients A, a correspond to the interval $\omega > f_*$, whereas B, b and B', b' correspond to $\omega < f$ (cf. (5.7)).

6. Concluding remarks

In this paper we have investigated inertial wave excitation and wave attractors in a rotating annular cavity, whose inner wall is a truncated cone (frustum). Waves were excited by longitudinal libration of (i) the frustum or (ii) the lids together with the outer cylinder. The set-up was investigated by boundary-layer analysis, by ray tracing, by DNS and by measurements in the laboratory.

Up to weakly nonlinear regimes ($\varepsilon \lesssim 0.2$) inertial waves could be clearly identified. They manifest themselves most notably by characteristic beams that are excited in the corners, as well as spatial structures corresponding to wave attractors and, for some distinct frequencies, periodic orbits. We showed examples of low-order wave attractors and periodic orbits exhibited by DNS, observations and ray tracing. Qualitative agreement was found between the results of all three methods. For the same parameters, DNS and observations yielded remarkable similarities, to be seen, for instance, in the wave beam widths.

It should be noted that DNS and measurements also exhibited a steady prograde mean flow layer located at $r = r_1(z = 0)$ that spanned the entire height. Its origin is nonlinearity in the Ekman layer along the librating frustum or the librating lids, respectively. The prograde mean flow layer is surprisingly persistent throughout the entire wave band even though it is a feature of the asymptotic limit without inertial waves (for $\omega > f$ see Sauret & Le Dizès 2013; for $\omega \to 0$ see Wang 1970 and Busse 2010).

Inertial waves were dominantly excited locally in the corners of the annular cavity. This coincides with the results published recently by Boisson *et al.* (2012) and Sauret *et al.* (2012), as well as experiments by Beardsley (1970) and McEwan (1970). Our geometry is closer to the configuration studied by Swart *et al.* (2010), who studied inertia-gravity waves excited by libration in a large annulus with a sloping inner wall.

Applying existing boundary-layer theory revealed that an Ekman layer forms over a librating wall that is inclined by an angle $\alpha \neq 0$ to the axis of rotation. We showed

that both the Ekman layer depth δ'_- and Ekman pumping velocity w'_E exhibit a strong and qualitatively similar dependency on the forcing frequency ω. The Ekman layers forming over the librating frustum ($\alpha < \pi/2$) or a librating lid ($\alpha = \pi/2$) differ in their eruption frequencies and boundary-layer depths, but the boundary-layer structure is identical (see figure 10, curves for $\delta'_\pm$ and $\delta_\pm$).

Simulations revealed that kinetic energy of the non-resonantly excited bulk wave field exhibits the same frequency dependence as the kinetic energy in the oscillating Ekman layer after subtracting a constant term representing libration, i.e. $K^{bulk}_{\omega,nr}(\omega) \propto K^E_\omega(\omega) - K_{lib}$. This was shown for the case of frustum in libration in figure 12 and for the case of lids plus outer cylinder in libration in figure 13. The bulk wave energy for non-resonant frequencies is given by the Ekman pumping energy, i.e. $K^{bulk}_{\omega,nr} \propto \hat{w}^2_E(\omega)$, where $\hat{w}_E$ denotes the amplitude of the Ekman pumping velocity.

Inspecting the wave excitation mechanism further revealed that the inclined librating surface induces an oscillating wall-tangential Ekman flux balanced by a wall-normal influx (Ekman pumping/suction). Close to the corners in the (r, z)-plane, we found a mismatch in the wall-tangential mass fluxes in the numerical simulations (figure 11) as inferred from linear boundary-layer theory. Both, discontinuity of the wall velocity (see figure 11*b*, comparing the curves for corners A and D) and nonlinearity emerging in the boundary layer (anharmonic content seen in figure 11), enhance this flux discrepancy. Owing to geometric constraints, this discrepancy is balanced by an outflow roughly directed along the bisectrix. Inertial waves are thus efficiently excited in the corner regions. However, how the dispersion relation is met locally is not yet fully understood.

It is worth mentioning that the energy spectra shown in figures 12 and 13 are reminiscent of internal wave spectra found in the ocean. Figures 7 and 8 of Munk (1980) exhibit a peak at the local inertial frequency (the so-called 'inertial cusp') and show qualitatively similar decay rates as our spectra in figures 12 and 13. A pole of the form $|f^2_* - \omega^2|^{-1/2}$ arises. In our work this is similar (see (5.7)), but is related to Ekman pumping/suction induced by the librating frustum or lid.

Enhancement of bulk flow amplitudes was observed for structures corresponding to low-order wave attractors or periodic orbits obtained by ray tracing. A viscous line broadening of about $\delta\omega/\Omega_0 \approx 0.05$ was observed that resulted in quasi-resonant excitations. To which degree this can be attributed only to viscosity (frequency shift and finite beam widths) or also to boundary-layer effects (Lopez & Marques 2014) was not investigated here.

Simulations confirm that the Stokes layer over the librating outer cylinder plays a minor role with respect to wave excitation. Without induced secondary layers on the lids, the Stokes layer is unable to excite inertial waves. This is because it entirely consists of an azimuthal flow and no volume flux component is directed towards the corners in the (r, z)-plane. Yet it is amazing that the Stokes layer can contain orders of magnitude larger kinetic energy than the Ekman layers or the interior wave field, which can be seen in figure 13.

Wave excitation efficiency was defined by the ratio $K^{bulk}_\omega / K^{BL}_\omega$. It can be interpreted as a coupling factor of the boundary layer and bulk flow, where K^{BL}_ω denotes the sum over all oscillating boundary layers. We suggest that spectral power input is proportional to the kinetic energy in the oscillating boundary layers. Simulation results shown in figure 14 revealed that wave excitation is most efficient when the oscillating Ekman layer erupts and when resonance occurs. This holds equally for the librating lid and for the librating frustum. Resonant excitations can increase the excitation efficiency by an order of magnitude.

By the present study we could demonstrate that the annular geometry with an inner frustum offers the possibility to study internal shear layers, wave attractors and wave excitation relevant for planetary flows in a somewhat simpler set-up than a spherical shell. It is an archetype configuration that supports an azimuthal mean flow and provides focusing of inertial waves at the inclined inner wall. The possibility to have different walls librating has proven useful since it allowed us to separate effects at the sloping inner and vertical outer wall from those at the lids.

Acknowledgements

This work is part of the project 'Mischung und Grundstromanregung durch propagierende Trägheitswellen: Theorie, Experiment und Simulation', financed by the German Science Foundation (DFG). The authors wish to thank Hans-Jakob Kaltenbach for providing a documented version of the incompressible Navier–Stokes solver for axisymmetric diffuser flow. The construction work of Patrick Lemke and the technical help by Steffen Fischer, Hans-Jürgen Pflanz, Paul Schäfer, Robin Stöbel and Yongtai Wang is kindly acknowledged. We also thank the anonymous reviewers for their critical remarks that helped to improve the quality of the final version.

Appendix A. Generalized coordinates and pressure treatment

In this section the transformation of the Navier–Stokes equations into generalized curvilinear coordinates is briefly summarized for the purpose of implementation in a numerical solver (cf. § 2.2). We apply covariant notation and Einstein's summation convention to any twice-appearing index regardless of its position. We make use of the general framework of curvilinear coordinates (see for instance Schade 1997) to derive equations in terrain-following coordinates.

We begin with introducing a set of covariant curvilinear coordinates for the flow domain, i.e. $(\xi^1, \xi^2, \xi^3) \mapsto (x, y, z)$ with (x, y, z) denoting the underlying Cartesian coordinates. Then $\boldsymbol{r}$ denotes the position vector independent of a particular basis. Due to the mapping, bounding walls coincide with coordinate surfaces, e.g. $\xi^1 = 0, 1$ and $\xi^2 = 0, 1$ in the case of an annular cavity. For a bundle of coordinate lines the associated covariant and contravariant basis vectors of the dual basis are

$$\boldsymbol{a}_i = \frac{\partial \boldsymbol{r}}{\partial \xi^i} \quad \text{and} \quad \boldsymbol{a}^i = \nabla \xi^i. \tag{A 1a,b}$$

They need not to be of unit length, but we require them to be orthonormal in a holonomic sense $\boldsymbol{a}_i \cdot \boldsymbol{a}^j = \delta_i^j$ (see Schade 1997), where δ_i^j is the usual Kronecker symbol (summation is suppressed for $i = j$). In order to minimize the number of metric terms we exploit axial symmetry by the mapping

$$x = r(\xi^1, \xi^2)\cos\varphi(\xi^3), \quad y = r(\xi^1, \xi^2)\sin\varphi(\xi^3), \quad z = z(\xi^1, \xi^2), \tag{A 2a–c}$$

where $r^2 = x^2 + y^2$ is the polar radius in the (x, y)-plane, $\varphi = \xi^3 \in [0, 2\pi)$ is the azimuthal angle and z is the direction of the axis. The associated Jacobi matrix reads

$$\frac{\mathrm{D}(x, y, z)}{\mathrm{D}(\xi^1, \xi^2, \xi^3)} = (\boldsymbol{a}_1, \boldsymbol{a}_2, \boldsymbol{a}_3) = \begin{pmatrix} \tilde{c}_1^{1/2}\cos\varphi & \tilde{c}_2^{1/2}\cos\varphi & -\tilde{c}_3^{1/2}\sin\varphi \\ \tilde{c}_1^{1/2}\sin\varphi & \tilde{c}_2^{1/2}\sin\varphi & \tilde{c}_3^{1/2}\cos\varphi \\ c_1^3 & c_2^3 & 0 \end{pmatrix}, \tag{A 3}$$

with the quasi-two-dimensional curvilinear components in the (r, z)-plane

$$\tilde{c}_1^{1/2} \equiv \frac{\partial r}{\partial \xi^1}, \quad \tilde{c}_2^{1/2} \equiv \frac{\partial r}{\partial \xi^2}, \quad \tilde{c}_3^{1/2} \equiv r, \quad c_1^3 \equiv \frac{\partial z}{\partial \xi^1}, \quad c_2^3 \equiv \frac{\partial z}{\partial \xi^2}. \tag{A 4a–e}$$

The covariant components of the metric tensor g_{ij} can be obtained from the Jacobi matrix, i.e. $g_{ij} = c_i^k c_j^k$. Using properties of the holonomic basis it can be shown that the covariant and contravariant components are connected by

$$g^{il} = \frac{1}{J^2}\left(g_{jm}g_{kn} - g_{jn}g_{km}\right) \quad \text{for } (ijk) = (123) \text{ and } (lmn) = (123), \tag{A 5}$$

where (123) denotes a cyclic permutation and $J = \det(c_j^i) = \sqrt{g}$ is the Jacobian of the transformation. Defining $\beta^{ij} \equiv Jg^{ij}$ and $\gamma_j^i \equiv \beta^{ik}c_j^k$, which are both proportional to the inverse Jacobi matrix, aids stating the governing equations in a more compact form.

Velocities are replaced by volume fluxes q^i, which are parallel to the curvilinear coordinate lines (ξ^1, ξ^2, ξ^3). The chain rule reveals that contravariant components q^i are connected with Cartesian velocities v^k by $q^i = \gamma_k^i v^k$, where it should be noted that $v^k = v_k$. Contracting Cartesian components of (2.2) with γ_j^i (over j) and applying the chain rule yields

$$\begin{aligned}\frac{\partial q^i}{\partial t} = &-Ro\frac{1}{J}\gamma_j^i\frac{\partial}{\partial \xi^k}\left(\frac{1}{J}c_m^j q^m q^k\right) - \frac{2}{J}\left(\gamma_2^i c_m^1 q^m - \gamma_1^i c_n^2 q^n\right)\\ &-\beta^{il}\frac{\partial p}{\partial \xi^l} + \frac{1}{J}\gamma_j^i\frac{\partial}{\partial \xi^m}\left[E\beta^{mn}\frac{\partial}{\partial \xi^n}\left(\frac{1}{J}c_k^j q^k\right)\right],\end{aligned} \tag{A 6}$$

$$0 = \frac{\partial q^m}{\partial \xi^m}. \tag{A 7}$$

Note that axisymmetry with respect to the z-axis is used, which can be seen in the Coriolis term that possesses only fixed lower indices 1 and 2. Moreover, it can be shown for holonomic bases that $\partial\gamma_j^i/\partial\xi^i = 0$, which is the geometrical conservation law (Thompson, Warsi & Mastin 1985, p. 104). For a generic grid this may no longer be fulfilled in a discrete sense. Therefore, conservative and non-conservative derivatives were carefully used in accordance with the type of the derivative operators (cf. Morinishi *et al.* 1998). On substitution of γ_j^i and β^{ij} into (A 6) and (A 7), followed by an expansion of all sums, one can obtain the forms finally implemented. It is due to axial symmetry that several terms collapse in this step. Also note that the equations in this form require only three additional metric quantities to be stored in the (r, z)-plane, e.g. J, $\tilde{c}_j^i$ and β^{ij}.

The last step is the transformation of boundary conditions. Due to periodicity in azimuthal direction volume fluxes and pressure have to fulfill periodic Dirichlet conditions at the planes $\xi^3 = 0, 2\pi$. In the (r, z)-plane no-slip conditions apply at the surrounding walls. We restrict ourselves to wall-parallel motions of the wall. The wall velocity $\boldsymbol{v}_w$ thus fulfills $\boldsymbol{n}\cdot\boldsymbol{v}_w = 0$ with $\boldsymbol{n}$ the surface normal ($\boldsymbol{\nabla}\cdot\boldsymbol{v}_w = 0$ implied). Boundary values for the volume fluxes are easily obtained by mapping the prescribed wall velocity components to volume fluxes, i.e. $q^i = \gamma_j^i v^j$. For (2.5), (2.6) and (2.7) we have

$$q^1 = q^2 = 0, \quad q^3 = \frac{J}{\tilde{c}_3^{2/3}}v_\varphi \quad \text{at } \xi^1 = 0, 1 \text{ and } \xi^2 = 0, 1, \tag{A 8a,b}$$

where only v_φ is non-zero on a librating wall. Pressure boundary conditions are obtained by insertion of $\boldsymbol{v}_w$ into the momentum balance. For walls at rest we obtain

$\partial p/\partial n = 0$, whereas on librating walls $\partial p/\partial n = -2(\boldsymbol{n} \times \boldsymbol{e}_z) \cdot \boldsymbol{v}_w$. For the discretized equations we use the fractional-step method (e.g. Perot 1993) computing the pressure in such a way that $\boldsymbol{v}$ is divergence-free at the end of every time step. In a discrete sense, pressure is never calculated precisely at the wall so that one-sided differences are used in the momentum balance. Neumann-type boundary conditions are moved into the discrete pressure field (pseudo-pressure formulation). The advantage is that only $\partial p/\partial n = 0$ needs to be implemented, which aids mass conservation because the momentum balance is skipped along the boundaries. In generalized coordinates we have

$$\frac{\partial p}{\partial \xi^1} = 0 \quad \text{at } \xi^1 = 0, 1, \qquad \frac{\partial p}{\partial \xi^2} = 0 \quad \text{at } \xi^2 = 0, 1. \tag{A 9a,b}$$

Note in this respect that the residual of the Poisson equation arising is modified only by the prescribed wall velocities. It might be worth noting that the pseudo-pressure (gradient) is also the physical pressure (gradient) on the lids ($\boldsymbol{n} = \pm\boldsymbol{e}_z$) and in the limit $\varepsilon \to 0$.

An important aspect of any incompressible solver is that the pressure has to adjust instantly to the velocity field so that the latter is solenoidal at all times. The fractional-step method is used to enforce this property over the time integration (see, e.g., Le & Moin 1991; Rosenfeld, Kwak & Vinokur 1991; Perot 1993). The third- and second-order temporal accuracies obtained with the Runge–Kutta and Crank–Nicolson schemes are in this regard sufficient, since it was shown by Perot (1993) that the fractional-step scheme is limited to second-order accuracy due to its construction. In our implementation the azimuthal direction is treated spectrally such that the dynamic fields are Fourier-transformed in a first step. This yields a set of 2D Helmholtz problems for the different azimuthal wavenumbers. Each of them is solved directly by LU decomposition. In order to save CPU time, the equation for each azimuthal wavenumber is evaluated only if the corresponding residual exceeds a certain threshold. After that the fields are transformed back into the configuration space. By this procedure the constant pressure offset is regauged in each time step by pinning the zero-pressure level at a particular point in space, preferably near a non-librating wall to keep variations small. Nevertheless, the mean pressure level 'floats' and absolute pressure values have no physical meaning.

Finally, we would like to note that the code can also be used to simulate a full cylinder by using boundary conditions of Akselvoll & Moin (1996) at the axis. Axially periodic and axial inflow/outflow conditions are also readily implemented.

Appendix B. Geometrical approximations for the generalized coordinate framework

Discretization by finite differences requires a structured grid within the trapezoid ABCD (cf. figure 1*a*). The grid we used is depicted in figure 3 and was produced with an in-house two-dimensional algebraic grid generator. The azimuthal direction is equispaced, its construction hence straightforward.

The aspect ratios of the frustum and the gap are $r_1(0)/h = 1/5$ and $\Delta r(0)/h = 1/5$ respectively. Due to the holonomic constraint (locally orthogonal grid lines), smooth slope transitions had to be introduced near the lids at $z = 0, 1$. We chose these of length $\Delta z = 0.04$, yielding the 'matching height' $z_m = \Delta z$ in figure 3(*b*) and $z_m = 1 - \Delta z$ in figure 3(*c*). The shape function of the frustum, $r_1(z)$, is required to be at least two times continuously differentiable to avoid metric artifacts from the viscous term. We used

$$r_1(z) = r_1(1) + \left[1 - F_{\Delta z}(z)\right]\left[r_1(0) - r_1(1)\right], \tag{B 1}$$

where $F_{\Delta z}(z)$ denotes a ramp function on the unit interval with smooth transitions at its ends, i.e.

$$F_{\Delta z}(z) = \begin{cases} CG\left(\dfrac{z}{2\Delta z}\right) & \text{for } 0 \leqslant z \leqslant \Delta z \\ C\left[1/2 + G'(1/2)\,\dfrac{z-\Delta z}{2\Delta z}\right] & \text{for } \Delta z < z < 1-\Delta z \\ C\left[G'(1/2)\,\dfrac{1-2\Delta z}{2\Delta z} + G\left(\dfrac{z-1+2\Delta z}{2\Delta z}\right)\right] & \text{for } 1-\Delta z \leqslant z \leqslant 1 \end{cases} \quad \text{(B 2)}$$

with the scale factor $C = [1 + G'(1/2)(1-2\Delta z)/(2\Delta z)]^{-1}$. The polynomial ramp $G(\xi)$ of lowest possible order that fulfills the geometrical requirements reads $G(\xi) = 6\xi^5 - 15\xi^4 + 10\xi^3$ for $\xi \in [0, 1]$. Its derivative is $G'(\xi) \equiv \mathrm{d}G(\xi)/\mathrm{d}\xi$.

The modification of the geometry resulted in a slight discrepancy between the inclination angles of the frustum in the laboratory ($\alpha_{lab} = 5.71°$) and that in the numerical grid ($\alpha_{num} = 5.93°$). As can be seen in figure 3(*b*,*c*) the error is largest near the inner top and bottom corners, but is only of the order of one grid cell. The mismatch in the inclination angles can be considered lesser a problem since inertial waves preserve the angle to the rotation axis upon reflection, whereas viscosity (here $E \gtrsim 10^{-6}$) overcompensates any sensible bias in the focusing reflections. Modification of geometry in the vicinity of the top and bottom inner corners along the frustum gives the most significant portion of the discretization error. This error cannot be resolved by increasing the resolution, but the modified geometry is self-consistent upon change in resolution.

Appendix C. Frequency filtering of numerical data

In order to separate features of stationary solution according to their time scales, a Fourier filter was applied to the numerical data. Filtered data was used for the figures 12–14.

A numerical simulation was performed for a certain libration frequency ω and a time series was stored from $t = t_0$ on, at which the system reached practically stationarity. For convenience, time slices were equispaced and taken for an integer number of libration periods $MT_{lib} = 2\pi M/\omega$ ($M = 1, 2, \ldots$). In the linear limit and for weakly nonlinear configurations filtering of only a few harmonic frequencies $l\omega$ with $l\omega \leqslant 2\Omega_0$ is sufficient. Projection amplitudes a_l, b_l that preserve the scales are obtained by evaluation of the discretized Fourier integrals

$$a_l = \frac{2}{MT_{lib}} \int_{t_0}^{t_0+MT_{lib}} g(t)\cos(l\omega t)\,\mathrm{d}t \approx \frac{2}{N}\sum_{j=0}^{N-1} g(t_j)\cos\frac{2\pi jl}{N}, \quad \text{(C 1)}$$

$$b_l = \frac{2}{MT_{lib}} \int_{t_0}^{t_0+MT_{lib}} g(t)\sin(l\omega t)\,\mathrm{d}t \approx \frac{2}{N}\sum_{j=0}^{N-1} g(t_j)\sin\frac{2\pi jl}{N}. \quad \text{(C 2)}$$

Integration is done for every grid point $\boldsymbol{r}_i$ and for all variables so that formally $g(t_j) = (\boldsymbol{v}, p, \ldots)^{\mathrm{T}}(\boldsymbol{r}_i, t_j)$. Amplitudes A_l and phases θ_l are obtained via $A_l = (a_l^2 + b_l^2)^{1/2}$ and $\theta_l = \arctan(b_l/a_l)$ for $l \geqslant 1$ and with $\theta_l \in [-\pi, \pi)$. For the mean ($l = 0$) we have $A_0 = \sum_j g(t_j)/N$ and $\theta_0 \equiv 0$. Spatial structures seen in the fields $A_l(\boldsymbol{r})$ and $\theta_l(\boldsymbol{r})$, however, consist of several wave vectors that fulfill the dispersion relation for ω_l.

Appendix D. Power input by libration and its effect on the flow

The observed fluid flow state inside the cavity for the given (longitudinal) libration frequency ω is not perfectly time-coherent, but is weakly chaotic (turbulent) and the individual wave trains may have a characteristic life-duration time of the order of dominating wave period, $2\pi/\omega$. The period $2\pi/\omega$ is supposed to be short in comparison with the spin-up time determined by the harmonic mean between the rotation period $2\pi/\Omega_0 \equiv 4\pi/f$ (Coriolis parameter $f = 2\Omega_0$) and the diffusion time along the height $h = 2H$ of the approximately cylindrical cavity (Greenspan & Howard 1963; Busse 2011). It means that $\omega/f \gg \delta_E/H \sim 3 \times 10^{-3}$, in our experiment and numerical simulations.

The power input by libration can be derived by applying a modification of the 'fastest response principle' to our fluid system. It means that the destruction of kinetic energy K of the flow in the fluid interior occurs on the shortest time-scale permissible in the system, in our case ω^{-1} (a shorter time scale f^{-1} should be excluded from considerations, because it specifies the Ekman layer formation rate (Greenspan & Howard 1963), whereas the boundary layer internal dynamics are eventually responsible for the destruction of the energy K). So, any variation in ω, say $\delta\omega$, leads to the corresponding variation in the (kinetic) energy destruction rate $K\delta\omega$. The later quantity must be equilibrated by the corresponding variation in the external mechanical power P input to the system, which yields

$$K\delta\omega = \delta P. \tag{D 1}$$

Changing from variations to differentials we obtain

$$K(\omega) = \frac{\mathrm{d}P}{\mathrm{d}\omega}(\omega). \tag{D 2}$$

In the following, we use the notation with respect to the bottom lid axes (see figure 1*b*) and we replace $f_* \to f$ throughout. As a substitute for $P(\omega)$ in the right-hand side of (D 2) we use the power input through the librating lids by taking the product of the velocity of librations, $u|_{z=0} = \varepsilon(f/2)r\sin\omega t$, and the calculated surface stress in the oscillating Ekman boundary layer, i.e. $\rho\nu(\partial u/\partial z)|_{z=0}$. Integration of the horizontal vorticity ζ by exploiting axisymmetry (see (5.4)–(5.6)) yields for the azimuthal velocity component

$$\begin{aligned} u = {} & \frac{\varepsilon f r}{4}\left(\mathrm{sgn}[f_* - \omega]\mathrm{e}^{-z/\delta_-}\sin\frac{z}{\delta_-} - \mathrm{e}^{-z/\delta_+}\sin\frac{z}{\delta_+}\right)\cos\omega t \\ & + \frac{\varepsilon f r}{4}\left(\mathrm{e}^{-z/\delta_-}\cos\frac{z}{\delta_-} + \mathrm{e}^{-z/\delta_+}\cos\frac{z}{\delta_+}\right)\sin\omega t. \end{aligned} \tag{D 3}$$

With this, the product of wall velocity and surface stress is integrated over the whole lid, averaged over the period $2\pi/\omega$ and, finally, the result is taken with the opposite sign (to fulfill the third Newton law demands). The mechanical power introduced into the fluid via longitudinal librations of the outer cylinder wall plays a less important role in determining the flow dynamics in the fluid main bulk (including inertial wave oscillations) and is disregarded in our estimates (cf. Wang 1970; Busse 2011). So, the power input corresponding to each lid reads

$$P(\omega) = \frac{\pi}{32\sqrt{2}}\rho\nu^{1/2}\varepsilon^2 f^{5/2}\left(r_2^4 - r_1^4\right)F(\omega/f) \tag{D 4}$$

with r_1 and r_2 denoting the inner and outer radius, respectively, and

$$F(\xi) = \begin{cases} \sqrt{1+\xi} - \sqrt{1-\xi} & \text{for } \xi < 1, \\ \sqrt{\xi+1} + \sqrt{\xi-1} & \text{for } \xi > 1. \end{cases} \tag{D 5}$$

When $\omega/f \ll 1$ then $P \propto \omega$, while $P \propto \omega^{1/2}$ in the opposite limit case of $\omega/f \gg 1$. There is a $(\mathrm{d}P/\mathrm{d}\omega)$-singularity at $\omega/f = 1$ (boundary layer eruption over the librating lid; cf. figure 10). The calculation and conclusion also applies to the frustum in libration with formally substituting $f \to f_* \equiv f \sin\alpha$.

From (D 2) and (D 4) and by summing contributions from the top and bottom lids (the cavity is approximately considered as purely cylindrical) one gets

$$K(\omega) \equiv \rho \frac{U^2(\omega)}{2} \pi \left(r_2^2 - r_1^2\right) 2H = \frac{\mathrm{d}P(\omega)}{\mathrm{d}\omega} \equiv \frac{\pi}{16\sqrt{2}} \rho \nu^{1/2} \varepsilon^2 f^{3/2} \left(r_2^4 - r_1^4\right) \frac{\mathrm{d}F(\omega/f)}{\mathrm{d}(\omega/f)}. \tag{D 6}$$

In the low-frequency limit $\omega/f \ll 1$ one thus has the estimate

$$U^2 \approx \frac{1}{8} \nu^{1/2} \varepsilon^2 f^{3/2} \frac{r_2^2 + r_1^2}{H} \sim 2.1 \times 10^{-6}\ \mathrm{m}^2\ \mathrm{s}^{-2}, \tag{D 7}$$

i.e. (D 7) predicts velocities $U \sim 10^{-3}$ m s^{-1} that are of the order of experimentally measured values and numerical solutions. Typically, simulated and measured values are in the order of 2 mm s^{-1} for the parameters considered, where the laboratory data referred to were obtained recently by PIV measurements in the laboratory. Note that these velocities constitute a small fraction, in the order of $(\delta_E/H)^{1/2}$, of the libration velocity amplitude $U_0 = \varepsilon(f/2)r_2$ (here at the outer cylinder). Under the same limit $\omega/f \ll 1$ and in comparison with the vertical velocity amplitude at the top of the oscillating Ekman boundary layer, i.e. $\hat{w}_E \approx \varepsilon\sqrt{2\nu f}/2$ (cf. (5.7)), (D 7) predicts $(H/\delta_E)^{1/2}$-times larger values.

Equation (D 6) describes satisfactorily the frequency dependence of experimental results for both situations, librating frustum and the librating outer cylinder plus lids. The plot of function $\mathrm{d}F(\omega/f)/\mathrm{d}(\omega/f)$ is qualitatively similar to that of the oscillating Ekman depth $\delta'_- \equiv \sqrt{2\nu/|f_* - \omega|}$ in figure 10 and is not presented here.

REFERENCES

AGRAWAL, B. N. 1993 Dynamic characteristics of liquid motion in partially filled tanks of a spinning spacecraft. *J. Guid. Control Dyn.* **16**, 636–640.

AKSELVOLL, K. & MOIN, P. 1996 An efficient method for temporal integration of the Navier–Stokes equations in confined axisymmetric geometries. *J. Comput. Phys.* **125** (2), 454–463.

ALDRIDGE, K. D. & TOOMRE, A. 1969 Axisymmetric inertial oscillations of a fluid in a rotating spherical container. *J. Fluid Mech.* **37** (2), 307–323.

BATCHELOR, G. K. 1967 *An Introduction to Fluid Dynamics*. Cambridge University Press.

BEARDSLEY, R. C. 1970 An experimental study of inertial waves in a closed cone. *Stud. Appl. Maths* **49**, 187–196.

BOISSON, J., LAMRIBEN, C., MAAS, L. R. M., CORTET, P.-P. & MOISY, F. 2012 Inertial waves and modes excited by the libration of a rotating cube. *Phys. Fluids* **24**, 076602.

BORCIA, I. D. & HARLANDER, U. 2012 Inertial waves in a rotating annulus with inclined inner cylinder: comparing the spectrum of wave attractor frequency bands and the eigenspectrum in the limit of zero inclination. *Theor. Comput. Fluid Dyn.* **27**, 397–413.

BORDES, G., VENAILLE, A., JOUBAUD, S., ODIER, P. & DAUXOIS, T. 2012 Experimental observation of a strong mean flow induced by internal gravity waves. *Phys. Fluids* **24** (8), 086602.

BUSSE, F. H. 2010 Mean zonal flows generated by librations of a rotating spherical cavity. *J. Fluid Mech.* **650**, 505–512.

BUSSE, F. H. 2011 Zonal flow induced by longitudinal librations of a rotating cylindrical cavity. *Physica* D **240** (2), 208–211.

BUSSE, F. H., DORMY, E., SIMITEV, R. & SOWARD, A. M. 2007 *Mathematical Aspects of Natural Dynamos*. Grenoble Sciences and CRC Press.

CALKINS, M. A., NOIR, J., ELDREDGE, J. D. & AURNOU, J. M. 2010 Axisymmetric simulations of libration-driven fluid dynamics in a spherical shell geometry. *Phys. Fluids* **22** (8), 086602.

CANUTO, C., HUSSAINI, M. Y., QUARTERONI, A. & ZANG, T. A. 1991 *Spectral Methods in Fluid Dynamics*. Springer.

CHOI, H. 1993 Turbulent drag reduction: studies of feedback control and flow over riblets. PhD thesis, Stanford University.

CHOI, H., MOIN, P. & KIM, J. 1993 Direct numerical simulations of turbulent-flow over riblets. *J. Fluid Mech.* **255**, 503–539.

CORTET, P.-P., LAMRIBEN, C. & MOISY, F. 2010 Viscous spreading of an inertial wave beam in a rotating fluid. *Phys. Fluids* **22**, 086603.

CZARNY, O., SERRE, E., BONTOUX, P. & LUEPTOW, R. M. 2003 Interaction between Ekman pumping and the centrifugal instability in Taylor–Couette flow. *Phys. Fluids* **15** (2), 467–477.

DOMINGUEZ-LERMA, M. A., AHLERS, G. & CANELL, D. S. 1985 Effects of 'Kalliroscope' flow visualization particles on rotating Couette–Taylor flow. *Phys. Fluids* **28**, 1204–1206.

EMERY, W. J. & THOMSON, R. E. 2001 *Data Analysis Methods in Physical Oceanography*. Elsevier.

GOSTIAUX, L. & DAUXOIS, T. 2007 Laboratory experiments on the generation of internal tidal beams over steep slopes. *Phys. Fluids* **19** (2), 028102.

GREENSPAN, H. P. 1969 *The Theory of Rotating Fluids*, Cambridge Monographs on Mechanics and Applied Mathematics. Cambridge University Press, Reprint with corrections.

GREENSPAN, H. P. & HOWARD, L. N. 1963 On a time-dependent motion of a rotating fluid. *J. Fluid Mech.* **17**, 385–404.

GRIGULL, U., STRAUB, J. & SCHIEBENER, P. 1990 *Steam Tables in SI-Units/Wasserdampftafeln*. Springer.

HARLANDER, U. & MAAS, L. R. M. 2006 Characteristics and energy rays of equatorially trapped, zonally symmetric internal waves. *Meteorol. Z.* **15**, 439–450.

HARLANDER, U. & MAAS, L. R. M. 2007*a* Internal boundary layers in a well mixed equatorial atmosphere/ocean. *Dyn. Atmos. Oceans* **44**, 1–28.

HARLANDER, U. & MAAS, L. R. M. 2007*b* Two alternatives for solving hyperbolic boundary value problems of geophysical fluid dynamics. *J. Fluid Mech.* **588**, 331–351.

HENDERSON, G. A. & ALDRIDGE, K. D. 1992 A finite-element method for inertial waves in a frustum. *J. Fluid Mech.* **234**, 317–327.

JOUVE, L. & OGILVIE, G. I. 2014 Direct numerical simulations of an inertial wave attractor in linear and nonlinear regimes. *J. Fluid Mech.* **745**, 223–250.

KALTENBACH, H.-J., FATICA, M., MITTAL, R., LUND, T. S. & MOIN, P. 1999 Study of flow in a planar asymmetric diffuser using large-eddy simulation. *J. Fluid Mech.* **390**, 151–185.

KERSWELL, R. R. 1995 On the internal shear layers spawned by the critical regions in oscillatory Ekman boundary layers. *J. Fluid Mech.* **298**, 311–325.

KOCH, S., HARLANDER, U., EGBERS, C. & HOLLERBACH, R. 2013 Inertial waves in a spherical shell induced by librations of the inner sphere: experimental and numerical results. *Fluid Dyn. Res.* **45** (3), 035504.

LE, H. & MOIN, P. 1991 An improvement of fractional step methods for the incompressible Navier–Stokes equations. *J. Comput. Phys.* **92** (2), 369–379.

LIGHTHILL, J. 1978 *Waves in Fluids*. Cambridge University Press.

LOPEZ, J. M. & MARQUES, F. 2011 Instabilities and inertial waves generated in a librating cylinder. *J. Fluid Mech.* **687**, 171–193.

LOPEZ, J. M. & MARQUES, F. 2014 Rapidly rotating cylinder flow with an oscillating sidewall. *Phys. Rev.* E **89**, 013013.

MAAS, L. R. M. 2001 Wave focusing and ensuing mean flow due to symmetry breaking in rotating fluids. *J. Fluid Mech.* **437**, 13–28.

MAAS, L. R. M. 2005 Wave attractors: linear yet nonlinear. *Intl J. Bifurcation Chaos* **15** (9), 2757–2782.

MAAS, L. R. M. & HARLANDER, U. 2007 Equatorial wave attractors and inertial oscillations. *J. Fluid Mech.* **570**, 47–67.

MAAS, L. R. M. & LAM, F.-P. A. 1995 Geometric focusing of internal waves. *J. Fluid Mech.* **300**, 1–41.

MAAS, L. R. M. & VAN HAREN, J. J. M. 1987 Observations on the vertical structure of tidal and inertial currents in the central North Sea. *J. Mar. Res.* **45**, 293–318.

MANDERS, A. M. M. & MAAS, L. R. M. 2003 Observations of inertial waves in a rectangular basin with one sloping boundary. *J. Fluid Mech.* **493**, 59–88.

MATISSE, P. & GORMAN, M. 1984 Neutrally buoyant anisotropic particles for flow visualization. *Phys. Fluids* **27**, 759–760.

MCEWAN, A. D. 1970 Inertial oscillations in a rotating fluid cylinder. *J. Fluid Mech.* **40** (3), 603–640.

MESSIO, L., MORIZE, C., RABAUD, M. & MOISY, F. 2008 Experimental observation using particle image velocimetry of inertial waves in a rotating fluid. *Exp. Fluids* **44**, 519–528.

MOIN, P. & MAHESH, K. 1998 Direct numerical simulation: a tool in turbulence research. *Annu. Rev. Fluid Mech.* **3030**, 539–578.

MORINISHI, Y., LUND, T. S., VASILYEV, V. O. & MOIN, P. 1998 Fully conservative higher order finite difference schemes for incompressible flow. *J. Comput. Phys.* **143** (1), 90–124.

MUNK, W. H. 1980 Internal wave spectra at the buoyant and inertial frequencies. *J. Phys. Oceanogr.* **10**, 1718–1728.

NOIR, J., CALKINS, M. A., LASBLEIS, M., CANTWELL, J. & AURNOU, J. M. 2010 Experimental study of libration-driven zonal flows in a straight cylinder. *Phys. Earth Planet. Inter.* **182**, 98–106.

NOIR, J., HEMMERLIN, F., WICHT, J., BACA, S. M. & AURNOU, J. M. 2009 An experimental and numerical study of librationally driven flow in planetary cores and subsurface oceans. *Phys. Earth Planet. Inter.* **173**, 141–152.

ORLANDI, P. 2000 *Fluid Flow Phenomena – A Numerical Toolkit*. Kluwer.

OTT, E. 1993 *Chaos in Dynamical Systems*. Cambridge University Press.

PEROT, J. B. 1993 An analysis of the fractional step method. *J. Comput. Phys.* **108**, 51–58.

PHILLIPS, O. M. 1963 Energy transfer in rotating fluids by reflection of inertial waves. *Phys. Fluids* **6** (4), 513–520.

PRANDLE, D. 1982 The vertical structure of tidal currents and other oscillatory flows. *Cont. Shelf Res.* **1** (2), 191–207.

RIEUTORD, M., GEORGEOT, B. & VALDETTARO, L. 2001 Inertial waves in a rotating spherical shell: attractors and asymptotic spectrum. *J. Fluid Mech.* **435**, 103–144.

RIEUTORD, M. & VALDETTARO, L. 1997 Inertial waves in a rotating spherical shell. *J. Fluid Mech.* **341**, 77–99.

ROSENFELD, M., KWAK, D. & VINOKUR, M. 1991 A fractional step solution method for the unsteady incompressible Navier–Stokes equations in generalized coordinate systems. *J. Comput. Phys.* **94** (1), 102–137.

SAURET, A., CÉBRON, D. & LE BARS, M. 2013 Sponateous generation of inertial waves from boundary turbulence in a librating sphere. *J. Fluid Mech.* **728**, R5.

SAURET, A., CÉBRON, D., LE BARS, M. & LE DIZÈS, S. 2012 Fluid flows in a librating cylinder. *Phys. Fluids* **24**, 026603.

SAURET, A. & LE DIZÈS, S. 2013 Libration-induced mean flow in a spherical shell. *J. Fluid Mech.* **718**, 181–209.

SCHADE, H. 1997 *Tensoranalysis*. Walter de Gruyter.

SMIRNOV, S. A., BAINES, P. G., BOYER, D. L., VOROPAYEV, S. I. & SRDIC-MITROVIC, A. N. 2005 Long-time evolution of linearly stratified spin-up flows in axisymmetric geometries. *Phys. Fluids* **17**, 016601.

SWART, A., MANDERS, A., HARLANDER, U. & MAAS, L. R. M. 2010 Experimental observation of strong mixing due to internal wave focusing over sloping terrain. *Dyn. Atmos. Oceans* **50**, 16–34.

THOMPSON, J. E., WARSI, Z. U. A. & MASTIN, C. W. 1985 *Numerical Grid Generation: Foundations and Applications*. North-Holland.

THORADE, H. 1928 Gezeitenuntersuchungen in der Deutschen Bucht der Nordsee. *Deutsche Seewarte* **46** (3), 1–85. Friedrichsen, de Gruyter & Co.

TILGNER, A. 2007 Zonal wind driven by inertial modes. *Phys. Rev. Lett.* **99** (19), 194501.

TILGNER, A. 2009 Rotational dynamics of the core. In *Treatise in Geophysics*, vol. 8. Elsevier.

VERZICCO, R. & ORLANDI, P. 1996 A finite-difference scheme for three-dimensional incompressible flows in cylindrical coordinates. *J. Comput. Phys.* **123** (2), 402–414.

WANG, C.-Y. 1970 Cylindrical tank of fluid oscillating about a state of steady rotation. *J. Fluid Mech.* **41**, 581–592.

ZHANG, K., CHAN, K. H., LIAO, X. & AURNOU, J. M. 2013 The non-resonant response of fluid in a rapidly rotating sphere undergoing longitudinal libration. *J. Fluid Mech.* **720**, 212–235.